



UNIVERSITÀ POLITECNICA DELLE MARCHE
Repository ISTITUZIONALE

Entropy conserving implicit time integration in a Discontinuous Galerkin solver in entropy variables

This is the peer reviewed version of the following article:

Original

Entropy conserving implicit time integration in a Discontinuous Galerkin solver in entropy variables / Colombo, A; Crivellini, A; Nigro, A. - In: JOURNAL OF COMPUTATIONAL PHYSICS. - ISSN 0021-9991. - 472:(2023). [10.1016/j.jcp.2022.111683]

Availability:

This version is available at: 11566/314174 since: 2024-09-21T13:48:01Z

Publisher:

Published

DOI:10.1016/j.jcp.2022.111683

Terms of use:

The terms and conditions for the reuse of this version of the manuscript are specified in the publishing policy. The use of copyrighted works requires the consent of the rights' holder (author or publisher). Works made available under a Creative Commons license or a Publisher's custom-made license can be used according to the terms and conditions contained therein. See editor's website for further information and terms and conditions.

This item was downloaded from IRIS Università Politecnica delle Marche (<https://iris.univpm.it>). When citing, please refer to the published version.

(Article begins on next page)

Entropy conserving implicit time integration in a Discontinuous Galerkin solver in entropy variables

A. Colombo^a, A. Crivellini^{b,*}, A. Nigro^b

^a *University of Bergamo,
Department of Engineering and Applied Sciences*

^b *Marche Polytechnic University,
Department of Industrial Engineering and Mathematical Sciences*

Abstract

This article presents a fully discrete entropy conserving/stable method based on a Discontinuous Galerkin (DG) discretization in entropy variables coupled with a modified Crank-Nicolson scheme. The entropy conserving time integration is inspired by the work of LeFloch [1], originally developed in the context of a Finite Volume method in conservative variables. This entropy conserving time integrator is here adapted to a DG discretization in entropy variables also demonstrating the fulfilment of entropy conservation regardless of the time step size and the type of elements used (quadrangular or triangular elements, possibly with curved edges). The performance of the implicit method will be demonstrated by computing several inviscid flow problems, *i.e.*, the convection of an isentropic vortex, the double shear layer, the Kelvin-Helmholtz instability, the shedding flow past a triangular wedge, the Sod shock tube, the receding flow and the Taylor-Green vortex.

Keywords: Discontinuous Galerkin, generalized Crank-Nicolson, entropy conserving/stable discretizations, entropy variables.

1. Introduction

1 **1. Introduction**
2 This paper presents an entropy conserving method for the numerical solution
3 of the Euler equations in the context of a high-order Discontinuous Galerkin (DG)
4 discretization. Hyperbolic systems of partial differential equations (PDEs), such as
5 the one describing the behaviour of compressible inviscid flows, can admit several

*Corresponding author: a.crivellini@staff.univpm.it, Tel +39 0712204436

6 weak solutions. To properly select the physical relevant one an entropy function
7 can be defined. This function is constant where the solution is smooth and it can
8 only increase across singularities such as shock waves. The idea to embed this
9 physical constraint in the numerical method is not new, see for example the seminal
10 works of Tadmor *et al.* [2, 3], but has received increasing attention in recent years,
11 in particular when applied in the context of high-order DG methods. This class
12 of numerical methods is very attractive for Computational Fluid Dynamics (CFD)
13 thanks to the ability to get high-accuracy on unstructured and hybrid grids [4] and
14 the favourable dissipation and dispersion proprieties that makes DG well suited to
15 the scale-resolving simulation of turbulent flows, *e.g.*, [5, 6, 7].

16 DG discretizations with entropy conserving capabilities usually follow two ap-
17 proaches: *i*) the use of Summation by Parts (SBP) operators, split forms of the Eu-
18 ler equations and the conservative set of variables, see the works of Gassner *et al.*,
19 *e.g.*, [8, 9]; *ii*) the use of a symmetrized form of the governing equations together
20 with the set of entropy variables. The latter method, employed in this work, does
21 not introduce any limitation at the continuum level but it requires to “exactly” eval-
22 uate all the integrals part of the discrete form. This can be numerically achieved
23 by means of *over-integration*, *i.e.*, by computing integrals using quadrature for-
24 mulas with a degree of exactness large enough to make negligible the integration
25 errors of non-polynomial functions, see [10]. When numerical methods that use
26 a piecewise discontinuous representations of the solution are considered, properly
27 designed numerical flux functions that guarantee entropy conservation/stability
28 must be used, see for example [11, 12, 13]. Most of them were proposed in the
29 context of low-order Finite Volume (FV) entropy conserving schemes. Space-time
30 DG methods can also be considered to devise entropy conserving schemes. How-
31 ever, in the authors’ opinion, such approach is impractical, as all the time slabs
32 are linked together by a centred temporal state (numerical flux in time), *e.g.* see
33 Friedrich *et al.* [14]. For this reason, the method of lines is here considered, which
34 implies the use of numerical fluxes and time integration schemes both having en-
35 tropy conserving properties.

36 While the development of specifically designed numerical fluxes has been the
37 subject of several works, less attention has been devoted in literature to the develop-
38 ment of entropy conserving time integrators. Recent articles from Lozano [15, 16]
39 show that, for a generic entropy function, explicit and fully implicit Runge-Kutta
40 schemes introduce spurious entropy. The papers also indicate the Backward-Euler
41 method as an entropy stable scheme, *i.e.*, the entropy evolution in time is mono-
42 tone. Gouasmi *et al.* [17] also show that for both the BDF2 and the explicit
43 Leap-Frog methods it is difficult to determine a priori the sign of entropy pro-

44 duction, while the explicit Forward Euler scheme is entropy unstable. In Colombo
45 *et al.* [10] no clear statement about the entropy production of the linearly implicit
46 Runge-Kutta schemes of the Rosenbrock type was given. Note that, differently
47 from [15, 16, 17], in [10] the spatial discretization is based on a DG method with
48 entropy variables and not on more “standard” FV spatial approximations.

49 Up to the authors knowledge, the only entropy conserving scheme available in
50 the literature is a modified version of the Crank-Nicolson method. This modified
51 scheme is due to LeFloch *et al.* [1] and is often refereed as “*Generalized Crank-*
52 *Nicolson*” method. The scheme was originally developed in the context of FV
53 but is considered impractical as it requires numerical quadrature to assemble the
54 modified intermediate state which substitutes the algebraic mean in the residuals
55 vector evaluation of the standard scheme. Gouasmi *et al.* [17] proposed a compu-
56 tationally efficient implementation of the method by using theoretical arguments
57 which are very similar to those used in the development of entropy conserving
58 flux functions. It is worth mentioning that a similar idea was already proposed
59 in Subbareddy and Candler [18] to obtain a fully discrete FV scheme capable of
60 preserving kinetic energy.

61 The extension of these results to DG discretizations is not straightforward but
62 it can be considered of great interest. In fact, an efficient and high-order entropy
63 stable numerical framework that is also essentially dissipation-free in time, is an
64 excellent candidate for explicit LES as it allows a sharp control on the amount of
65 artificial dissipation added by the subgrid-scale model [19]. This paper will report
66 in detail how to implement the entropy conserving time integrator scheme in a DG
67 modal solver, in particular when entropy variables are used. The change of vari-
68 ables, in fact, involves a projection error that must be carefully taken into account.
69 Theoretical and numerical proofs will demonstrate that the approach is entropy
70 conserving in the sense that the L_2 -projection of the entropy variables on the con-
71 servative ones results in a “global” entropy conservation up to machine precision
72 irrespective of the time step size. The main features of the proposed method are:
73 *i)* the use of a couple of L_2 -projections between the entropy and the conservative
74 variables and vice versa; *ii)* to retain the time-derivative of the conservative vari-
75 ables in the governing equations instead of using the time derivative of the entropy
76 ones. This is done even though the solution is sought in terms of the degrees of
77 freedom of the entropy variables, a fundamental difference from the approach fol-
78 lowed by the authors in [10]. As in this work the conservation form of the Euler
79 equations is considered, feature *ii)* guarantees a conservative discretization.

80 In this paper, together with the implementation details of the method, numeri-
81 cal results for several test cases will be presented to assess the performance of the

82 entropy conserving framework regardless of the number and the type of elements,
 83 the spatial order of accuracy and the time step size. Results will be also presented
 84 for the entropy stable method, obtained by considering properly designed numerical
 85 flux functions, and for “standard” time-integration schemes.

86 2. The governing equations

87 The set of equations governing the behaviour of inviscid flows, *i.e.*, the Euler
 88 equations, can be written for the compressible case as

$$\begin{aligned}
 \frac{\partial \rho}{\partial t} + \frac{\partial}{\partial x_j} (\rho u_j) &= 0, \\
 \frac{\partial}{\partial t} (\rho u_i) + \frac{\partial}{\partial x_j} (\rho u_j u_i) &= -\frac{\partial p}{\partial x_i}, \\
 \frac{\partial}{\partial t} (\rho E) + \frac{\partial}{\partial x_j} (\rho u_j H) &= 0,
 \end{aligned} \tag{1}$$

89 where ρ is the fluid density, $\mathbf{u} = \{u_1, \dots, u_d\}$ the velocity vector, E and H the total
 90 energy and enthalpy, and $i, j = 1, \dots, d$, where d is the number of geometrical di-
 91 mensions. For a perfect gas, the pressure p is given by $p = (\gamma - 1) \rho [E - (u_i u_i)/2]$,
 92 where $\gamma = c_p/c_v$ is the ratio of gas specific heats, here set to 1.4. In compact form
 93 the system (1) can be written as

$$\frac{\partial \mathbf{q}}{\partial t} + \frac{\partial \mathbf{F}_i(\mathbf{q})}{\partial x_i} = \mathbf{0}, \tag{2}$$

94 with implied summation on index i and where $\mathbf{q} = \{\rho, \rho u_i, \rho E\}$ is the vector of the
 95 conservative variables and $\mathbf{F} \in \mathbb{R}^{2+d} \otimes \mathbb{R}^d$ is the convective flux function.

96 2.1. The entropy framework

97 The concept of entropy conservation relies on the existence of a convex func-
 98 tion, the *generalized entropy function* S , and the scalar-valued *entropy flux* func-
 99 tions \mathcal{U}_i , such that the following compatibility conditions holds

$$\frac{\partial S(\mathbf{q})}{\partial \mathbf{q}} \frac{\partial \mathbf{F}_i(\mathbf{q})}{\partial \mathbf{q}} = \frac{\partial \mathcal{U}_i(\mathbf{q})}{\partial \mathbf{q}} \quad \text{with} \quad i = 1, \dots, d. \tag{3}$$

100 By left-multiplying Eq. (2) by $\partial S(\mathbf{q})/\partial \mathbf{q}$ we obtain

$$\frac{\partial \mathcal{S}(\mathbf{q})}{\partial t} + \frac{\partial \mathcal{U}_i(\mathbf{q})}{\partial x_i} = 0, \quad (4)$$

101 with implied summation on index i . Since entropy needs to be dissipated at shock
 102 waves, the above identity is replaced by the following inequality

$$\frac{\partial \mathcal{S}(\mathbf{q})}{\partial t} + \frac{\partial \mathcal{U}_i(\mathbf{q})}{\partial x_i} \leq 0, \quad (5)$$

103 that, assuming periodic boundary conditions, can be integrated in space giving

$$\frac{d}{dt} \int_{\mathbb{R}^d} \mathcal{S}(\mathbf{q}) d\mathbf{x} \leq 0. \quad (6)$$

104 Note that \mathcal{S} differs from the common thermodynamic definition of entropy, which
 105 increases across shocks.

106 By assuming that \mathcal{S} is strictly convex, the mapping $\mathbf{q} \rightarrow \partial \mathcal{S}(\mathbf{q})/\partial \mathbf{q}$ can be
 107 regarded as a change of variables from the conservative variables \mathbf{q} to the entropy
 108 variables $\mathbf{v} = \partial \mathcal{S}(\mathbf{q})/\partial \mathbf{q}$. The system of governing equations (2) is symmetrized
 109 when rewritten in terms of entropy variables as

$$\frac{\partial \mathbf{q}(\mathbf{v})}{\partial \mathbf{v}} \frac{\partial \mathbf{v}}{\partial t} + \frac{\partial \mathbf{F}_i(\mathbf{q}(\mathbf{v}))}{\partial \mathbf{v}} \frac{\partial \mathbf{v}}{\partial x_i} = \mathbf{0}, \quad (7)$$

110 where $\partial \mathbf{q}(\mathbf{v})/\partial \mathbf{v}$ is positive-definite.

111 According to Huges *et al.* [20] the only *generalized entropy function-entropy*
 112 *flux pair*, up to a multiplicative constant, which symmetrizes the viscous term in
 113 the compressible Navier–Stokes equations is

$$\mathcal{S} = -\frac{\rho s}{\gamma - 1}, \quad \mathcal{U}_i = S u_i, \quad \text{whith } i = 1, \dots, d, \quad (8)$$

114 where $s = \ln(p\rho^{-\gamma})$ is the thermodynamic entropy. The corresponding set of en-
 115 tropy variables is

$$\mathbf{v} = \left\{ \frac{\gamma - s}{\gamma - 1} - \frac{\rho}{2p} |\mathbf{u}|^2, \frac{\rho u_i}{p}, -\frac{\rho}{p} \right\}. \quad (9)$$

116 Since $\partial \mathbf{q}(\mathbf{v})/\partial \mathbf{v}$ and $\partial \mathbf{F}_i(\mathbf{q}(\mathbf{v}))/\partial \mathbf{v}$ are symmetric, there exists an *entropy potential*,
 117 ϑ , *entropy flux potential*, ψ_i , pair such that $\partial \vartheta/\partial \mathbf{v} = \mathbf{q}(\mathbf{v})$ and $\partial \psi_i/\partial \mathbf{v} = \mathbf{F}_i(\mathbf{q}(\mathbf{v}))$.
 118 It can be easily proved that $\vartheta = \mathbf{v} \cdot \mathbf{q}(\mathbf{v}) - \mathcal{S}(\mathbf{q}(\mathbf{v}))$ and $\psi_i = \mathbf{v} \cdot \mathbf{F}_i(\mathbf{q}(\mathbf{v})) - \mathcal{U}_i(\mathbf{q}(\mathbf{v}))$,

119 and that they reduce to $\vartheta = \rho$ and $\psi_i = \rho u_i$ when the generalized entropy function
 120 of Eq. (8) is used.

121 In this work, following the seminal work of Huges *et al.* [20], the system of
 122 governing equations (7) is solved by directly approximating the entropy variables
 123 \mathbf{v} in the discrete space. To fulfil entropy conservation at the discrete level, the
 124 approach assumes that integrals must be computed exactly [21]. However, this
 125 statement can be relaxed as shown in [10]. Indeed, numerical results demonstrate
 126 that if integrals are approximated by using “accurate enough” quadrature rules, the
 127 entropy conservation is verified.

128 3. The Generalized Crank-Nicolson scheme in the DG framework

129 In this work, when “standard” time integration schemes are considered, they
 130 are applied to the governing equations written in the following form

$$\frac{\partial \mathbf{q}(\mathbf{v})}{\partial \mathbf{v}} \frac{\partial \mathbf{v}}{\partial t} + \frac{\partial \mathbf{F}_i(\mathbf{q}(\mathbf{v}))}{\partial x_i} = \mathbf{0}. \quad (10)$$

131 By applying the classical Crank-Nicolson (SCN) scheme the system of semi-discrete
 132 governing equations becomes

$$\frac{\partial \mathbf{q}(\mathbf{v}^{n+1/2})}{\partial \mathbf{v}} \frac{\mathbf{v}^{n+1} - \mathbf{v}^n}{\Delta t} + \frac{\partial \mathbf{F}_i(\mathbf{q}(\mathbf{v}^{n+1/2}))}{\partial x_i} = \mathbf{0}, \quad (11)$$

133 where $\mathbf{v}^{n+1/2}$ is defined according to the algebraic mean of the working variables,
 134 *i.e.*, $1/2(\mathbf{v}^{n+1} + \mathbf{v}^n)$. Equation (11) is not in a conservative form due to the Jacobian
 135 of the change of variables, $\partial \mathbf{q}(\mathbf{v}^{n+1/2})/\partial \mathbf{v}$.

136 LeFloch *et al.* [1] designed the following entropy conserving time integration
 137 scheme

$$\frac{\mathbf{q}^{n+1} - \mathbf{q}^n}{\Delta t} + \frac{\partial \mathbf{F}_i(\mathbf{q}(\mathbf{v}^{n+1/2}))}{\partial x_i} = \mathbf{0}, \quad (12)$$

138 where

$$\mathbf{v}^{n+1/2}(\mathbf{q}^n, \mathbf{q}^{n+1}) = \int_0^1 \mathbf{v}((1 - \chi)\mathbf{q}^n + \chi\mathbf{q}^{n+1}) d\chi. \quad (13)$$

139 The scheme was proposed in the context of FV entropy conserving schemes for
 140 non-linear systems of equations. Following the Tadmor [2] terminology this method
 141 will be referred as “Generalized Crank-Nicolson” (GCN). It is proven that when

142 GCN is coupled with an entropy conserving flux function, the resulting FV dis-
 143 cretization is entropy conserving both in space and in time. However, it is not
 144 obvious how to extend this result to a high-order DG discretization in entropy
 145 variables. In fact, in Eq. (10) the set of working variables is not the conservative
 146 but the entropy one and the time derivative term is multiplied by the Jacobian ma-
 147 trix $\partial \mathbf{q}(\mathbf{v})/\partial \mathbf{v}$. Moreover, the projection between the entropy variables, \mathbf{v} , and the
 148 conservative ones, \mathbf{q} (and vice versa) involves an approximation error. To solve
 149 these issues Eq. (7) has been recast in the traditional conservative form as

$$\frac{\partial \mathbf{q}(\mathbf{v})}{\partial t} + \frac{\partial \mathbf{F}_i(\mathbf{v})}{\partial x_i} = \mathbf{0}, \quad (14)$$

150 where, with an abuse of notation, $\mathbf{F}_i(\mathbf{v})$ is used in place of $\mathbf{F}_i(\mathbf{q}(\mathbf{v}))$. The time
 151 discretization of Eq. (14) gives

$$\frac{\mathbf{q}(\mathbf{v}^{n+1}) - \mathbf{q}(\mathbf{v}^n)}{\Delta t} + \frac{\partial \mathbf{F}_i(\mathbf{v}^{n+1/2})}{\partial x_i} = \mathbf{0}. \quad (15)$$

152 The system of governing equations is now discretized in space by multiplying
 153 Eq. (15) by an arbitrary smooth test function $\mathbf{w} = \{w_1, \dots, w_{d+2}\}$ and integrat-
 154 ing by parts, to obtain the weak formulation of each k -th scalar equation

$$\begin{aligned} \int_{\Omega} w_k \frac{q_k(\mathbf{v}^{n+1}) - q_k(\mathbf{v}^n)}{\Delta t} d\Omega &= \int_{\Omega} \frac{\partial w_k}{\partial x_i} F_{k,i}(\mathbf{v}^{n+1/2}) d\Omega \\ &- \int_{\partial\Omega} w_k F_{k,i}(\mathbf{v}^{n+1/2}) n_i d\sigma, \end{aligned} \quad (16)$$

155 where $\Omega \in \mathbb{R}^d$, with $d \in \{2, 3\}$, is the domain, $\partial\Omega$ its boundary and $\mathbf{n} =$
 156 $\{n_1, \dots, n_d\}$ the unit vector normal to the boundary. In this work, when used as a
 157 subscript, the symbol k is an index spanning the range $1, \dots, 2 + d$, otherwise it
 158 will represent the degree of polynomial functions.

159 Denoting by $\mathcal{K}_h = \{K\}$ a mesh of the domain made of elements K , the solution
 160 in conservative, \mathbf{q} , and entropy, \mathbf{v} , variables, together with the test function \mathbf{w} , are
 161 replaced with finite element approximations, \mathbf{q}_h and \mathbf{v}_h , and a discrete test function
 162 \mathbf{w}_h , all of them belonging to the discrete polynomial space $[\mathbb{P}_d^k(\mathcal{K}_h)]^{2+d}$. Each
 163 component $q_{h,k}$ of the numerical solution can be expressed, in terms of the elements
 164 of the global vector \mathbf{Q} of unknown degrees of freedom, as $q_{h,k} = \phi_j Q_{k,j}$, with
 165 $j = 1, \dots, (N_{dof}) \text{ card}(\mathcal{K}_h)$, where $N_{dof} = \prod_{i=1,d} (k + i/i)$ and ϕ_j belongs to the
 166 set of orthogonal and hierarchical basis functions defined according to [4]. For the

167 sake of notation, the set $\mathcal{F}_h \stackrel{\text{def}}{=} \mathcal{F}_h^i \cup \mathcal{F}_h^b$ of mesh faces is defined, where \mathcal{F}_h^b collects
168 the faces lying on the boundary of Ω_h . For any $F \in \mathcal{F}_h^i$ there exist two elements
169 $K^+, K^- \in \mathcal{K}_h$ such that $F \in \partial K^+ \cap \partial K^-$. For all $F \in \mathcal{F}_h$, \mathbf{n}_F is the normal unit
170 vector pointing from K^+ to K^- , for the sake of notation compactness, the subscript
171 F will be dropped in the following. Since a function $w_h \in \mathbb{P}_d^k(\mathcal{K}_h)$ is double valued
172 over an internal face $F \in \mathcal{F}_h^i$, the jump trace operator $[[w_h]] \stackrel{\text{def}}{=} w_{h|K^+} - w_{h|K^-}$
173 is defined. This operator acts componentwise when applied to a vector. The DG
174 discretization of the Euler equations results in seeking, for $k = 1, \dots, 2+d$, the
175 elements of \mathbf{Q} such that

$$\begin{aligned} \sum_{K \in \mathcal{K}_h} \int_K \phi_i \phi_j \frac{Q_{k,j}^{n+1} - Q_{k,j}^n}{\Delta t} d\Omega &= \sum_{K \in \mathcal{K}_h} \int_K \frac{\partial \phi_i}{\partial x_l} F_{k,l} (\mathbf{v}_h^{n+1/2}) d\Omega \\ &- \sum_{F \in \mathcal{F}_h} \int_F [[\phi_i]] \hat{F}_k (\mathbf{v}_h^{\pm n+1/2}, \mathbf{n}) d\sigma. \end{aligned} \quad (17)$$

176 To demonstrate the conserving/stability properties of the present scheme we fo-
177 cus firstly on the discrete form of the unsteady term of Eq. (4) resulting from the
178 LHS of (17). $Q_{k,j}^n$ and $Q_{k,j}^{n+1}$ are evaluated as the L_2 -projection of the conservative
179 variables (computed according to the entropy variables) on the DG polynomial
180 space

$$Q_{k,i}^n = [(\mathbf{M}^K)^{-1}]_{i,j} \int_K \phi_j q_k(\mathbf{v}_h^n) d\Omega, \quad (18)$$

181 where $\mathbf{M}_{i,j}^K = \int_K \phi_i \phi_j d\Omega$ is the mass matrix of the element K . The projected
182 conservative variables $\hat{q} \in [\mathbb{P}_d^k(\mathcal{K}_h)]^{2+d}$ are then defined as

$$\hat{q}_{h,k}^n = \phi_j Q_{k,j}^n. \quad (19)$$

183 Similarly,

$$V_{k,i}^{n+1/2} = [(\mathbf{M}^K)^{-1}]_{i,j} \int_K \phi_j v_k^{n+1/2} d\Omega, \quad (20)$$

184 and

$$v_{h,k}^{n+1/2} = \phi_j V_{k,j}^{n+1/2}. \quad (21)$$

185 When $v_{h,k}^{n+1/2} = \phi_i V_{k,i}^{n+1/2}$ are used as the test functions in place of ϕ_i in Eq. (17),
 186 for each $K \in \mathcal{K}_k$ the unsteady term can be re-formulated as

$$\begin{aligned}
 & \int_K \phi_i V_{k,i}^{n+1/2} \phi_j \frac{Q_{k,j}^{n+1} - Q_{k,j}^n}{\Delta t} d\Omega = \left(\int_K \phi_i \phi_j d\Omega \right) V_{k,i}^{n+1/2} \frac{Q_{k,j}^{n+1} - Q_{k,j}^n}{\Delta t} = \\
 & = \mathbf{M}_{j,i}^K [(\mathbf{M}^K)^{-1}]_{i,m} \left(\int_K \phi_m v_k^{n+1/2} d\Omega \right) \frac{Q_{k,j}^{n+1} - Q_{k,j}^n}{\Delta t} = \\
 & = \delta_{j,m} \left(\int_K \phi_m v_k^{n+1/2} d\Omega \right) \frac{Q_{k,j}^{n+1} - Q_{k,j}^n}{\Delta t} = \int_K v_k^{n+1/2} \phi_j \frac{Q_{k,j}^{n+1} - Q_{k,j}^n}{\Delta t} d\Omega = \\
 & = \int_K v_k^{n+1/2} \frac{\hat{q}_{h,k}^{n+1} - \hat{q}_{h,k}^n}{\Delta t} d\Omega,
 \end{aligned} \tag{22}$$

187 where $\delta_{j,m}$ is the Kronecker delta function. The LeFloch's [1] identity states that

$$v_k^{n+1/2} \left(\hat{q}_{h,k}^{n+1} - \hat{q}_{h,k}^n \right) = S(\hat{\mathbf{q}}_h^{n+1}) - S(\hat{\mathbf{q}}_h^n), \tag{23}$$

188 and here it holds true pointwise if $\mathbf{v}^{n+1/2}$ is defined according to the projection of
 189 the entropy variables on the conservative set, *i.e.*, $\hat{\mathbf{q}}_h^n$ and $\hat{\mathbf{q}}_h^{n+1}$. In other words, Eq.
 190 (23) is valid when the intermediate state is

$$v_k^{n+1/2} (\hat{\mathbf{q}}_h^n, \hat{\mathbf{q}}_h^{n+1}) = \int_0^1 v_k \left((1 - \chi) \hat{\mathbf{q}}_h^n + \chi \hat{\mathbf{q}}_h^{n+1} \right) d\chi. \tag{24}$$

191 For the sake of compactness, in the following, $v_k^{n+1/2} (\hat{\mathbf{q}}_h^n, \hat{\mathbf{q}}_h^{n+1})$ will be denoted
 192 as $v_k^{n+1/2}$, accordingly, $\mathbf{v}^{n+1/2}$ was used in place of $\mathbf{v}^{n+1/2} (\mathbf{q}^n, \mathbf{q}^{n+1})$. Equation (24)
 193 implies that the last integral of Eq. (22) is equivalent to

$$\int_K \frac{S(\hat{\mathbf{q}}_h^{n+1}) - S(\hat{\mathbf{q}}_h^n)}{\Delta t} d\Omega, \tag{25}$$

194 which means that the PDE for the entropy evolution is implicitly discretized in a
 195 conservative form and the fully discrete scheme is entropy conserving. Moreover,
 196 since the conservative form of the governing equations is used, the scheme is fully
 197 conservative in time, *i.e.*, mass, momentum and energy are conserved at the dis-
 198 crete level. It is worth noting that $S(\mathbf{q}(\mathbf{v}_h^n))$ is different from $S(\hat{\mathbf{q}}_h^n)$. In fact, the
 199 peculiarity of the scheme is that while $V_{k,j}^{n+1}$ are the DOFs, the scheme is entropy

200 conserving in the sense that the projection on the conservative set is entropy con-
 201 serving, so the entropy solution is based on the $Q_{k,j}^{n+1}$ coefficients. However, during
 202 the simulations Eqs. (18) and (19) are only used for the evaluation of Eq. (24) since
 203 Eq. (22) is solved implicitly. Notice that, the L_2 -projection procedure does not alter
 204 the order of accuracy of the method, neither in space nor in time.

205 From the implementation point of view, Eq. (24) requires numerical integration
 206 and to properly select the degree of exactness of the quadrature rules to guarantee
 207 entropy conservation, a value difficult to be estimated *a priori*. A viable alter-
 208 native was proposed by Gouasmi *et al.* [17] who found a close form solution of
 209 Eq. (23). The idea behind this method is very similar to that used for the deriva-
 210 tion of entropy conserving numerical flux functions. The intermediate state $\mathbf{v}^{n+1/2}$
 211 of Gouasmi *et al.* is computed as

$$\begin{aligned}
 v_1^{n+1/2} &= \frac{1}{\gamma - 1} \left(\gamma \frac{\bar{\rho}}{\rho^{\ln}} - \bar{s}_h \right) - \overline{u_{i,h}} v_{1+i}^{n+1/2} - \frac{1}{2} \overline{u_{i,h} u_{i,h}} v_{2+d}^{n+1/2}, \\
 v_{1+i}^{n+1/2} &= -\overline{u_{i,h}} v_{2+d}^{n+1/2} \\
 v_{2+d}^{n+1/2} &= -\frac{\bar{\rho}_h}{p_h^{\ln}},
 \end{aligned} \tag{26}$$

212 where $i = 1, \dots, d$ and where $p_h = (\gamma - 1)[(\rho E)_h - (\rho u_i)_h (\rho u_i)_h / (2\rho_h)]$, $u_{i,h} =$
 213 $(\rho u_i)_h / \rho_h$ and $s_h = \ln(p_h \rho_h^{-\gamma})$ are evaluated using the projected solutions $\hat{\mathbf{q}}_h^n$ and
 214 $\hat{\mathbf{q}}_h^{n+1}$. The arithmetic and logarithmic means are defined as

$$\overline{a}_h = \frac{a_h^{n+1} + a_h^n}{2}, \quad \overline{a}_h^{\ln} = \frac{a_h^{n+1} - a_h^n}{\ln(a_h^{n+1}) - \ln(a_h^n)}. \tag{27}$$

215 Gouasmi *et al.* [17] also proved that the resulting scheme is second-order accurate
 216 in time. In the following this method will be denoted as GCNG. Here, thanks to
 217 the use of orthonormal shape functions, see [4] for the details, the implementa-
 218 tion strongly simplifies reducing the computational cost for the evaluation of the
 219 intermediate state $\mathbf{v}_h^{n+1/2}$.

220 Friedrich *et al.* [14] used a similar approach to derive an entropy conservative
 221 *temporal state* for their space-time DG algorithm. Their method takes advantage
 222 of the SBP property, it uses the conservative variable set and does not require
 223 *over-integration*. Their *temporal state* is essentially a central flux function defined
 224 in time that links together all the time slabs. The resulting space-time entropy

225 conservative scheme is not a real option since the only viable choice is a pure
 226 upwind *temporal state* which decouples the time slabs. However, in this case the
 227 scheme is “only” entropy stable.
 228 Concerning the RHS of (17), the linear combination with the coefficients $V_{k,i}^{n+1/2}$,
 229 where $k = 1, \dots, 2 + d$ and $i = 1, \dots, (N_{dof}) \text{ card}(\mathcal{K}_h)$, gives

$$\sum_{K \in \mathcal{K}_h} \int_K \frac{\partial v_k^{n+1/2}}{\partial x_l} F_{k,l}(\mathbf{v}_h^{n+1/2}) d\Omega - \sum_{F \in \mathcal{F}_h} \int_F \left[[v_{h,k}^{n+1/2}] \right] \hat{F}_k(\mathbf{v}_h^{\pm n+1/2}, \mathbf{n}) d\sigma. \quad (28)$$

230 By defining the potential flux as $\psi_l = v_k F_{k,l} - \mathcal{U}_l$, it can be shown that $\partial v_k / \partial x_l F_{k,l} =$
 231 $\partial \mathcal{U}_l / \partial x_l + \partial \psi_l / \partial x_l - v_k \partial F_{k,l} / \partial x_l$, cf. [21]. Moreover, since the compatibility con-
 232 dition holds, *i.e.*, $\partial \mathcal{U}_l / \partial x_l = v_k \partial F_{k,l} / \partial x_l$, it is possible to write $\partial v_k / \partial x_l F_{k,l} =$
 233 $\partial \psi_l / \partial x_l$. For the sake of notation compactness, in the above equation the de-
 234 pendence on $\mathbf{v}_h^{n+1/2}$ was omitted, and in the following the discrete potential flux
 235 $\psi_l(\mathbf{v}_h^{n+1/2})$ will be denoted as $\psi_{h,l}^{n+1/2}$. By substituting the previous result into Eq. (28)
 236 the following relation is obtained

$$\sum_{K \in \mathcal{K}_h} \int_K \frac{\partial \psi_{h,l}^{n+1/2}}{\partial x_l} d\Omega - \sum_{F \in \mathcal{F}_h} \int_F \left[[v_{h,k}^{n+1/2}] \right] \hat{F}_k(\mathbf{v}_h^{\pm n+1/2}, \mathbf{n}) d\sigma, \quad (29)$$

237 which, by using the divergence theorem, becomes

$$\sum_{F \in \mathcal{F}_h} \int_F \left[\left[[\psi_{h,l}^{n+1/2} n_l] \right] - \left[[v_{h,k}^{n+1/2}] \right] \hat{F}_k(\mathbf{v}_h^{\pm n+1/2}, \mathbf{n}) \right] d\sigma. \quad (30)$$

238 As an entropy conserving numerical flux function fulfils the following relation,
 239 cf. [21],

$$\left[[\psi_{h,l}^{n+1/2} n_l] \right] - \left[[v_{h,k}^{n+1/2}] \right] \hat{F}_k(\mathbf{v}_h^{\pm n+1/2}, \mathbf{n}) = 0, \quad (31)$$

240 Eq. (30) is identically zero and the scheme is entropy conserving in space. Simi-
 241 larly, using an entropy stable numerical flux where

$$\left[[\psi_{h,l}^{n+1/2} n_l] \right] - \left[[v_{h,k}^{n+1/2}] \right] \hat{F}_k(\mathbf{v}_h^{\pm n+1/2}, \mathbf{n}) \geq 0, \quad (32)$$

242 an entropy stable space DG discretization is obtained. Notice that, these results
 243 assume an exact evaluation of all the integrals. This result is not new, see [22], but
 244 it is here demonstrated on a different perspective. Together with Eq. (25) it proves

245 that the proposed method implicitly discretizes the entropy conservation/inequality
 246 of Eq. (6),

$$\begin{aligned} \sum_{K \in \mathcal{K}_h} \int_K \frac{S(\hat{\mathbf{q}}_h^{n+1}) - S(\hat{\mathbf{q}}_h^n)}{\Delta t} d\Omega = \\ \sum_{F \in \mathcal{F}_h} \int_F \left[\left[\left[\psi_{h,l}^{n+1/2} n_l \right] \right] - \left[\left[v_{h,k}^{n+1/2} \right] \right] \hat{F}_k \left(\mathbf{v}_h^{\pm n+1/2}, \mathbf{n} \right) \right] d\sigma \geq 0. \end{aligned} \quad (33)$$

247 Finally, the analogy between Eq. (31) and Eq. (23) highlights the similarity be-
 248 tween the entropy conserving flux functions, $\hat{\mathbf{F}}(\mathbf{v}_h^{\pm n+1/2}, \mathbf{n})$, and the intermediate
 249 state in time, $\mathbf{v}^{n+1/2}$.

250 3.1. Implementation details

251 Numerical integration of Eq. (17) by means of suitable Gauss quadrature leads
 252 to the following discrete system of non-linear equations

$$\mathbf{M} \frac{\mathbf{Q}(\mathbf{V}^{n+1}) - \mathbf{Q}(\mathbf{V}^n)}{\Delta t} + \mathbf{R}(\mathbf{V}^{n+1/2}) = \mathbf{0}, \quad (34)$$

253 where, according to Eq. (20) and Eq. (24) or Eq. (27), $\mathbf{V}^{n+1/2}$ is a non-linear func-
 254 tion of \mathbf{V}^{n+1} and \mathbf{V}^n .

255 Eq. (34) is here solved with a Newton-Kyrolv algorithm. For the sake of clarity,
 256 we will use here the notation $\mathbf{V}^{n+1/2} = \hat{\mathbf{V}}(\mathbf{V}, \mathbf{V}^n)$, where \mathbf{V} can be the actual solution
 257 vector of the Newton algorithm, $\mathbf{V}^{(i)}$, or the solution vector at the end of the time
 258 step, \mathbf{V}^{n+1} . The, possibly inexact, i -th Newton step finds $\Delta \mathbf{V}^{(i)} = (\mathbf{V}^{(i+1)} - \mathbf{V}^{(i)})$
 259 such that

$$\left(\frac{\mathbf{M}}{\Delta t} \frac{\partial \mathbf{Q}(\mathbf{V}^{(i)})}{\partial \mathbf{V}} + \frac{\partial \mathbf{R}}{\partial \hat{\mathbf{V}}} \frac{\partial \hat{\mathbf{V}}}{\partial \mathbf{V}} \right) \Delta \mathbf{V}^{(i)} = -\mathbf{M} \frac{\mathbf{Q}(\mathbf{V}^{(i)}) - \mathbf{Q}(\mathbf{V}^n)}{\Delta t} - \mathbf{R}, \quad (35)$$

260 where the dependence of \mathbf{R} and $\partial \mathbf{R} / \partial \hat{\mathbf{V}}$ on $\hat{\mathbf{V}}(\mathbf{V}^{(i)}, \mathbf{V}^n)$ was omitted for the sake of
 261 notation compactness.

262 The matrix $\partial \hat{\mathbf{V}} / \partial \mathbf{V}$ is a block-diagonal matrix which couples all the DOFs of
 263 an element and, particularly for the GCN, is not trivial to be derived and imple-
 264 mented. For this reason, this contribution to the implicit operator was approxi-
 265 mated as $(1/2)\mathbf{I}$, where \mathbf{I} is the identity matrix. The idea was to simply handle
 266 the term as in the standard Crank-Nicolson scheme. According to our numerical
 267 experiments, the impact of this approximation on the non-linear convergence was

268 small, *i.e.*, the number of non-linear steps required by GCN or GCNG to reach a
 269 full, machine precision, convergence was almost the same as for the SCN, which
 270 uses an exact Jacobian matrix. An example will be given in Sec. 4.1.

271 In all the implicit time integration schemes used in this paper, the Newton
 272 algorithm starts with $\mathbf{V}^{(1)} = \mathbf{V}^n$ and stops when $\|\Delta\mathbf{V}^{(k)}\|_{L^2}$ reaches the tolerance
 273 ε_{tol} . For the solution of the linear systems arising from both implicit and linearly
 274 implicit Rosenbrock-type schemes the preconditioned GMRES solvers available
 275 in the PETSc library are used [23].

276 4. Numerical results

277 The performance of the entropy conserving Crank-Nicolson scheme named
 278 GCNG in Sec. 3, in terms of accuracy of the solution and conservation property,
 279 has been assessed and compared to other time integrators, by computing the fol-
 280 lowing inviscid flow problems: *i*) the isentropic vortex; *ii*) the double shear layer;
 281 *iii*) the Kelvin-Helmholtz instability; *iv*) the shedding flow past a triangular wedge;
 282 *v*) the Sod shock tube; *vi*) the receding flow; *vii*) the Taylor-Green vortex. For the
 283 first flow problem, which has an exact analytical solution, the accuracy will be
 284 measured in terms of the η error, while the conservation properties, evaluated for
 285 several test cases, will be evaluated in terms of the ε error, which are defined as
 286 follows

$$\eta(\circ, \bullet_{ref}) = (\Omega_h)^{-1/2} \|\circ - \bullet_{ref}\|_{L^2}, \quad (36)$$

$$\varepsilon(\circ, \bullet_{ref}) = \Omega_h^{-1} \left(\int_{\Omega_h} \circ d\Omega - \int_{\Omega_h} \bullet_{ref} d\Omega \right), \quad (37)$$

287 where \circ and \bullet_{ref} are the numerical and the "reference" solutions, respectively. The
 288 reference value is set equal to the L_2 -projection of the initial solution on the DG
 289 polynomial space.

290 The results obtained with the GCN and/or the GCNG schemes will be com-
 291 pared with the computations from other time integrators. In particular, with the
 292 acronym BE we denote the first-order accurate Backward Euler scheme, with SCN
 293 the second-order accurate standard Crank-Nicolson scheme, with BDF2 the second-
 294 order accurate Backward Differentiation Formulae, with ROSXY the linearly-implicit
 295 Rosenbrock-type Runge-Kutta schemes, where X is the order of accuracy and Y is
 296 the number of stages, with RK35 the third-order accurate Strong Stability Preserv-
 297 ing explicit Runge-Kutta scheme with 5 stages, with FE the first-order accurate

298 explicit Forward Euler scheme. Details on the implementation and the efficient
299 use of Rosenbrock-type schemes in the DG framework can be found in [24, 25].

300 For all the simulations using implicit time integration schemes, to avoid any
301 influence of the time integration error, the non-linear solver tolerance ε_{tol} has been
302 set to 10^{-13} , whereas the linear solver tolerance has been set to 10^{-2} to speed-up
303 the iterative process. For the Rosenbrock-type schemes the iterative linear solver
304 tolerance was set equal to 10^{-13} .

305 To obtain a fully discrete entropy conserving/stable scheme, dedicated nu-
306 merical flux functions with entropy conserving/stable properties have been im-
307 plemented. In particular, the entropy conserving (EC) numerical flux of Ismail
308 and Roe [11], the kinetic energy preserving and entropy-conservative (KEEC) flux
309 of Chandrashekar [12], the entropy stable numerical flux based on the entropy-
310 consistent dissipation of Roe (ES), named EC1 in [11], and the entropy stable Go-
311 dunov flux computed from the exact solution of the Riemann problem (ERS) [26]
312 have been used. Following the findings of Colombo et al. [10], when simulations
313 are performed with the entropy preserving fluxes, *over-integration* must be con-
314 sidered to ensure entropy conservation. However, in the authors' experience, its
315 role becomes less relevant for simulations of simple flow problems that uses the
316 ES and ERS fluxes. In practice, all the computations shown in this paper were
317 performed using *over-integration*, with the exception of the isentropic vortex and
318 the double shear layer (on Cartesian grids) cases.

319 In the next sections, when reported, the elemental CFL number is defined as
320 $CFL_K = (|\mathbf{u}_a| + c_a)\Delta t/\Delta x_K$, where $c_a = \sqrt{\gamma p_a/\rho_a}$ is the speed of sound and
321 $\Delta x_K = d(V_K/S_K)$ is a measure of the cell size where V_K and S_K are the cell
322 volume (area when $d = 2$) and surface area (perimeter when $d = 2$), respectively.
323 The a subscript in the CFL definition means that variables are computed from
324 elemental mean values.

325 4.1. The isentropic vortex convection problem

326 The convection of an inviscid isentropic vortex [27, 28, 29] is here consid-
327 ered to assess the accuracy and the entropy conservation properties of the Crank-
328 Nicolson scheme named GCNG in Sec. 3, using the GCN scheme as reference.

329 The initial flow condition is given by

$$\begin{aligned}
 u_1 &= U - \frac{\alpha}{2\pi} \left(x_2 - \frac{L}{2} \right) e^{\beta(1-r^2)}, \\
 u_2 &= U + \frac{\alpha}{2\pi} \left(x_1 - \frac{L}{2} \right) e^{\beta(1-r^2)}, \\
 \Theta &= 1 - \frac{\alpha^2 (\gamma - 1)}{16\beta\gamma\pi^2} e^{2\beta(1-r^2)}, \\
 p &= 1,
 \end{aligned} \tag{38}$$

330 where Θ is the temperature and the “free-stream” non dimensional velocity com-
 331 ponents are equal to $U = \sqrt{\gamma}$, corresponding to a Mach number $M_\infty \approx 1.4$. The
 332 symbol r is the distance of a generic point of the computational domain of co-
 333 ordinates, (x_1, x_2) , with respect to the vortex center, placed in the middle of the
 334 computational domain. The α and β values are set equal to 5 and 1/2, respectively.
 335 The computational domain is $0 \leq x_i \leq L$, with $L = 10$, discretized with a fine
 336 and a coarse uniform mesh made of 50×50 and 25×25 quadrilateral elements,
 337 respectively. Boundary conditions are periodic and simulations are performed up
 338 to a final time T , corresponding to one period of vortex revolution.

339 Figure 1 shows a temporal convergence study performed using the fine grid, the
 340 \mathbb{P}^3 DG polynomial approximation and the EC flux. The largest time step size re-
 341 ported in the plots corresponds to $\text{CFL} \approx 3.8$. Figure 1(a) shows the performance
 342 of the two entropy conserving Crank-Nicolson schemes compared with other im-
 343 plicit and linearly-implicit temporal integrator showing that all of them achieve
 344 their formal order of accuracy. Moreover, for each of the time step size consid-
 345 ered, the schemes SCN, GCN and GCNG show the same η error values. As all the
 346 variables show similar behaviours, the η error for the first variable only is reported
 347 from now on. The ε error for ρs , reported in Fig. 1(b), shows that both the GCN
 348 and GCNG schemes reach the machine precision independently from the time step
 349 size, while all the other time integrators show convergence rates equal to or larger
 350 than the formal ones. The ε error is evaluated, for both the entropy conserving
 351 time integration schemes, by using the L_2 -projection of the entropy variables on
 352 the conservative ones, cf. Sec. 3. Due to the definition of ε , see Eq. (37), the con-
 353 vergence rates can be mainly ascribed to the dissipation error. The measured rates
 354 are order 3 for BDF2, and order 4 for SCN, while BE, ROS33 and ROS58 show a
 355 rate equal to the theoretical one, *i.e.*, 1, 3 and 5, respectively. For the GCN scheme
 356 a Gaussian quadrature rule corresponding to a very high degree of exactness (27)
 357 was used to compute the intermediate state of Eq (13) in order to guarantee the en-
 358 tropy conservation independently from the time step size. Although a comparison

359 of the computational effort for the different time integrators is beyond the scope
 360 of this section, it is clear that the GCN always requires a larger CPU time than the
 361 GCNG. In fact, the GCNG replaces the explicit quadrature by the evaluation of
 362 much cheaper algebraic formulae. For example, when considering the small time
 363 step size $\Delta t = T/2560$, the use of a third-degree accurate quadrature formula
 364 allows to reach the zero machine precision value of \mathcal{S} (\mathbb{P}^3 , fine grid, EC flux).
 365 However, even using this low-degree rule, the GCN is ≈ 1.7 times slower than the
 366 GCNG. Increasing the degree of exactness to 27, the safe choice suitable for very
 367 large Δt sizes, the CPU time becomes ≈ 5.5 times larger.

368 When comparing the performance of the GCNG and SCN schemes, a similar
 369 number of inexact Newton's iterations, 7 vs. 6, and almost the same CPU time, the
 370 GCNG is 5% faster, is measured. These values prove that the the computational
 371 cost needed by the GCNG to compute $\mathbf{V}^{n+1/2}$, corresponding to the 12.6% of the
 372 overall CPU time, is counterbalanced by the assembly and inversion of the change-
 373 of-variables matrix used by the SCN scheme, cf. Eq. (11) and Eq. (15). Although
 374 these results may vary considerably, *e.g.*, depending on the Δt size and the degree
 375 of the polynomial approximation, the same conclusion can be drawn: the proposed
 376 GCNG scheme can be less computationally demanding than a standard method,
 377 such as the SCN.

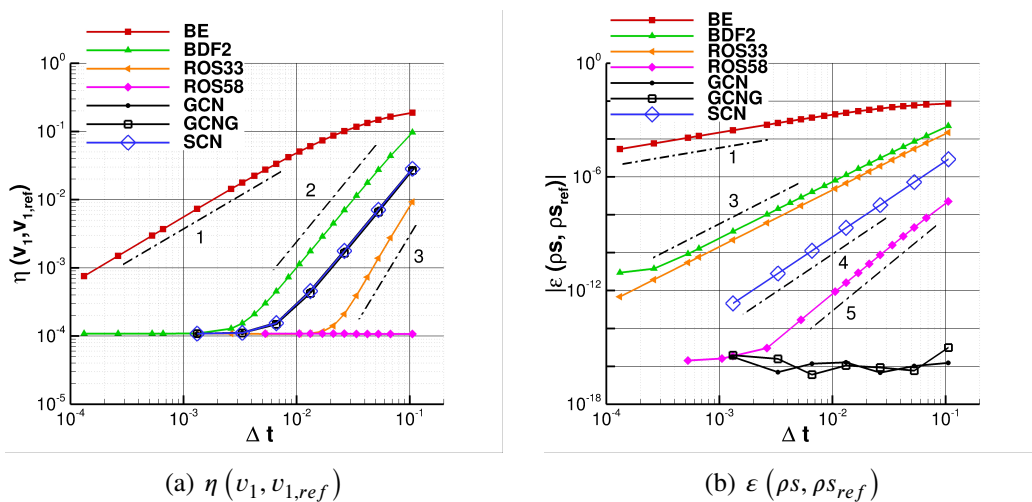


Figure 1: Isentropic vortex problem – Time refinement study. Simulations performed on the fine grid using the \mathbb{P}^3 DG approximation, the EC numerical flux and several time integration schemes.

378 Figure 2 shows a time refinement study for both the coarse and fine grids using
 379 the \mathbb{P}^3 approximation. In particular, Fig. 2(a) displays η computed for the first

380 conservative variable, q_1 , obtained through the L_2 -projection of the entropy set on
 381 the conservative one. For large time step sizes the computations on the two meshes
 382 show the same error values and achieve the formal order of accuracy of the scheme.
 383 When the time step is reduced the temporal error dominates the spatial one and
 384 different plateau values are reached. Notice that, the minimum error for q_1 on the
 385 fine mesh is lower than the one for v_1 shown in Fig. 1(a). The error on entropy in
 386 Fig. 2(b) is directly computed from the working variables and, as expected, does
 387 not verify the entropy preservation, although using a fully conserving scheme, cf.
 388 Sec. 3.

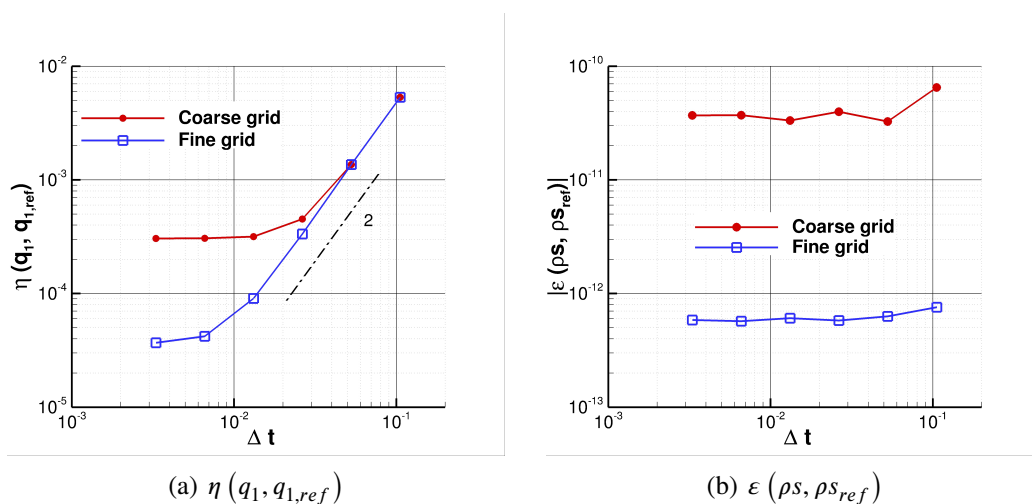


Figure 2: Isentropic vortex problem – Time refinement study. Simulations performed on the fine and the coarse grid using the \mathbb{P}^3 DG approximation, the EC numerical flux and the GCNG time integration scheme.

389 Figure 3 reports a time refinement study performed on the coarse grid using
 390 the \mathbb{P}^3 DG approximation and the entropy conserving and entropy stable numerical
 391 fluxes, EC and ES, respectively. In this plot the results from the GCNG method
 392 are compared with those from the ROS33 scheme. The simulations performed
 393 with the ES flux do not use *over-integration*. In fact, for this flow problem, it was
 394 observed that even using a large number of quadrature points leads to the same
 395 results. As expected, in Fig. 3, when the spatial error overwhelms the temporal
 396 one, the same plateau value for η is obtained by the different time integrators for
 397 a given numerical flux. Although for a large enough time step size the ROS33
 398 scheme reaches a significantly lower η error level than the GCNG, the linearly-
 399 implicit scheme cannot guarantee the entropy conservation for an arbitrary step

400 size but only for very small values, *i.e.*, when the temporal error is negligible with
 401 respect to the spatial one. On the contrary, the GCNG scheme reaches both the
 402 plateau values for ε , $\approx 10^{-7}$ for the ES flux and the machine precision for the
 403 EC flux, independently from the time step size, thus demonstrating the entropy
 404 preserving capability of the time integrator.

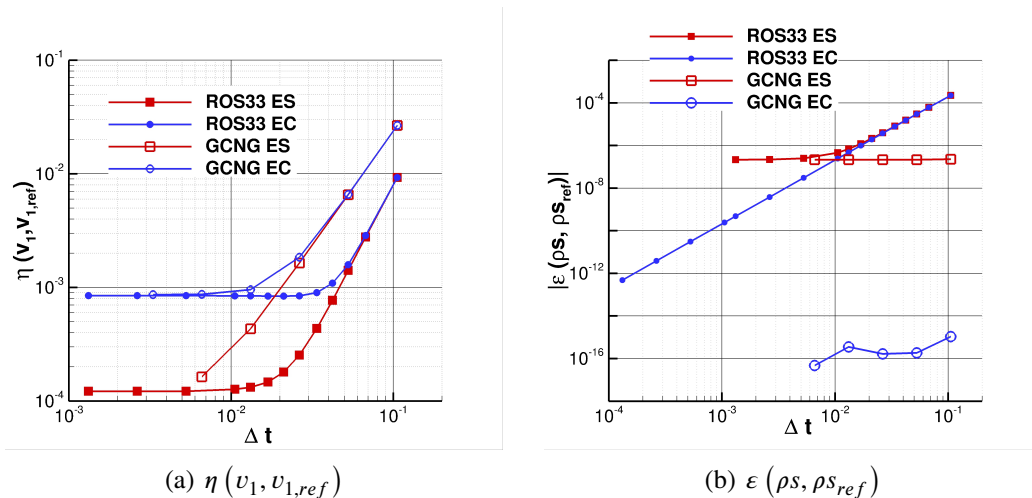


Figure 3: Isentropic vortex problem – Time refinement study. Simulations performed on the coarse grid using the \mathbb{P}^3 DG approximation, the EC and ES numerical fluxes and the ROS33 and the GCNG time integration schemes.

405 Based upon to the findings of this section, among the two generalized CN meth-
 406 ods considered in this work, only the GCNG scheme was used for the computation
 407 of the other test cases as it combines the entropy-conserving property with an af-
 408 fordable implementation suitable for production runs.

409 4.2. The inviscid double shear layer

410 The inviscid double shear layer [30, 31] flow problem is used to assess the con-
 411 servation properties of entropy, kinetic energy and enstrophy. The kinetic energy
 412 is defined as $\kappa = \rho u_i u_i / 2$, and the enstrophy as $\zeta = \omega^2$, where ω is the vorticity.
 413 Long time simulations performed with the GCNG time integration scheme, using
 414 different time step sizes and the EC and ES numerical fluxes, have been considered.

415 The initial flow condition is given by

$$\begin{aligned}
u_1 &= \begin{cases} U \tanh [(x_2 - \pi/2) / \delta_1] & \text{if } x_2 \leq \pi, \\ U \tanh [(3\pi/2 - x_2) / \delta_1] & \text{if } x_2 > \pi, \end{cases} \\
u_2 &= U \delta_2 \sin(x_1), \\
p &= 1, \\
\rho &= 1,
\end{aligned} \tag{39}$$

416 where $U = M_\infty \sqrt{\gamma}$, $\delta_1 = \pi/15$ and $\delta_2 = 0.05$, and, to obtain a nearly incompressible flow, $M_\infty = 0.01$. The computational domain $0 \leq x_i \leq 2\pi L$, with $L = 1$,
417 has been discretized by: *i*) a 8×8 uniform Cartesian mesh; *ii*) an anisotropic
418 and not uniform mesh made of 176 triangular elements; *iii*) a 8×8 mesh made of
419 quadrangular elements with curved parabolic edges. At all the boundaries periodic
420 conditions are imposed and the simulations are advanced in time up to $T = 80T_c$,
421 where $T_c = L/U$ is the convective time. The T_c value is ten times larger than the
422 one usually used in the literature.
423

424 Figure 4 shows the evolution in time of the errors on entropy, kinetic energy
425 and enstrophy for the Cartesian grid using the GCNG time integration scheme
426 coupled with the EC numerical flux and several time step sizes for the $\mathbb{P}^{3,4}$ DG
427 approximations. To quantify the errors related to enstrophy and kinetic energy
428 conservation, their relative percentage variation with respect to the reference value,
429 *i.e.*, $\varepsilon_r(\zeta, \zeta_{ref})\%$ and $\varepsilon_r(\kappa, \kappa_{ref})\%$, is monitored. Figure 4(a) shows an error on
430 entropy close to machine precision for any time step value, thus confirming the
431 entropy conserving capability of the GCNG scheme. Plots 4(b) and 4(c) reveal
432 that, for long time simulations, the even polynomial degree approximations show
433 a significant dissipation for both κ and ζ when compared to the odd case, this
434 odd/even effect was already observed and commented by the authors in [10]. This
435 behaviour contributes to a worse stability of \mathbb{P}^4 than \mathbb{P}^3 computations, as testified
436 by the divergent simulations for $\Delta t = T/200$ and $T/400$ (not shown in the plots).
437 Note that, the simulations performed with $\Delta t = T/800$, which is the larger time
438 step size for which both the odd and even DG approximations lead to a convergent
439 solution, corresponds to $\text{CFL} \approx 25$.

440 Furthermore, Fig. 4(b) shows that the relative percentage errors on kinetic energy
441 for the \mathbb{P}^3 solutions are almost constant for the different time step sizes con-
442 sidered. Differently, Fig. 4(c) shows that, for the same DG approximation \mathbb{P}^3 , the
443 relative percentage error on enstrophy is greater influenced by the time step size,
444 with error levels that are in the range [2%, 65%], except for the 160% value ob-
445 tained for the largest $\Delta t = T/200$ size.

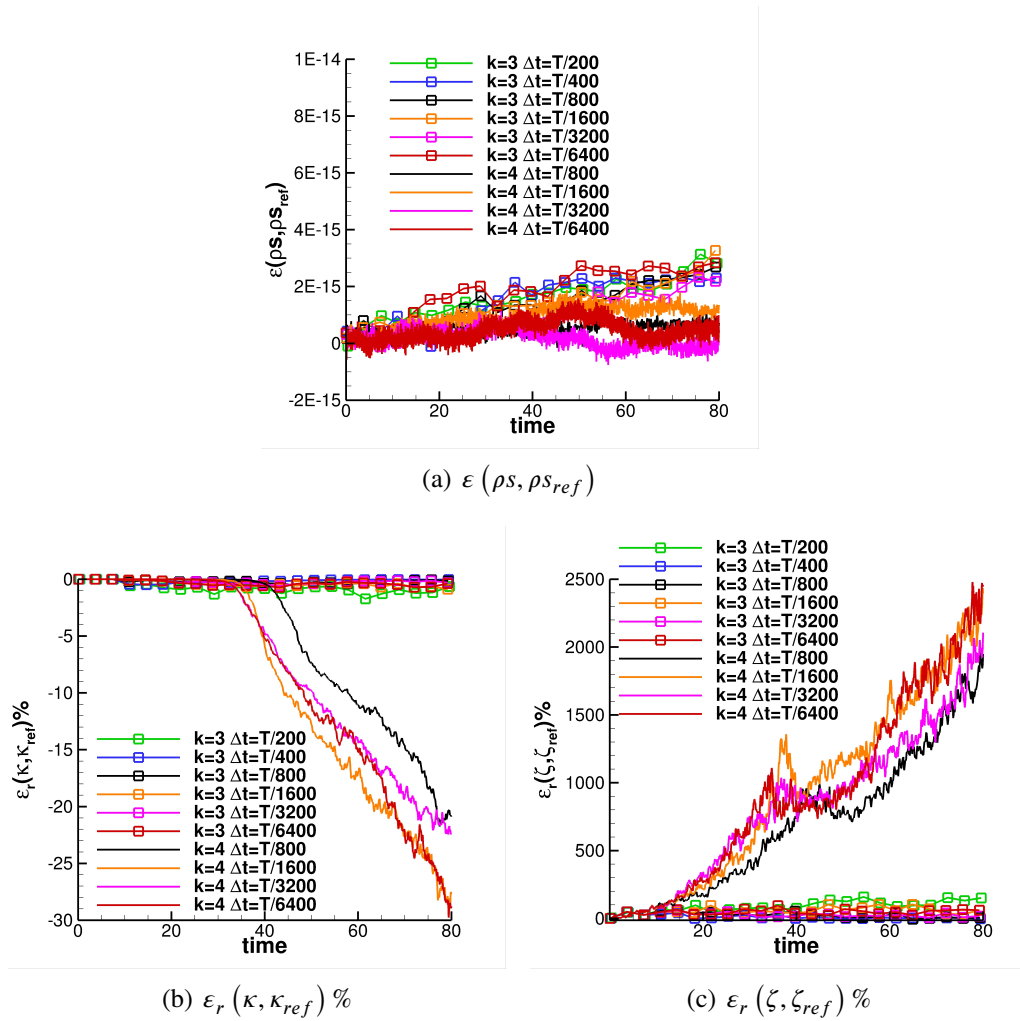


Figure 4: Double shear layers problem – Time refinement study. Simulations performed on the Cartesian grid using the $\mathbb{P}^{3,4}$ DG approximations, the EC numerical flux and the GCNG time integration scheme with different Δt values.

446 The same refinement study was performed by using the ES flux and results
 447 are summarized in Fig. 5. For the Cartesian grids only, entropy-stable simulations
 448 were performed without *over-integration* but verifying that a greater number of
 449 quadrature points led to the same results. As expected, cf. [10], computations are
 450 not affected by an odd/even effect and the $k = 4$ approximation shows, especially
 451 for entropy and kinetic energy, better conservation properties than the $k = 3$ case.
 452 Differently from the EC case, the use of the ES flux allowed to successfully perform

453 the computation for the $T/\Delta t = 200$ and $T/\Delta t = 400$ values.

454 When using the ES flux combined with the GCNG time integrator, the con-
 455 servation properties for a given DG approximation are roughly the same for all
 456 the time step sizes considered, thus further confirming the good properties of the
 457 GCNG. The pressure contours shown in Fig. 6 highlights the different level of ac-
 458 curacy achieved for the \mathbb{P}^4 DG approximation by using two different time steps
 459 sizes, *i.e.*, $T/\Delta t = 200$ and $T/\Delta t = 6400$.

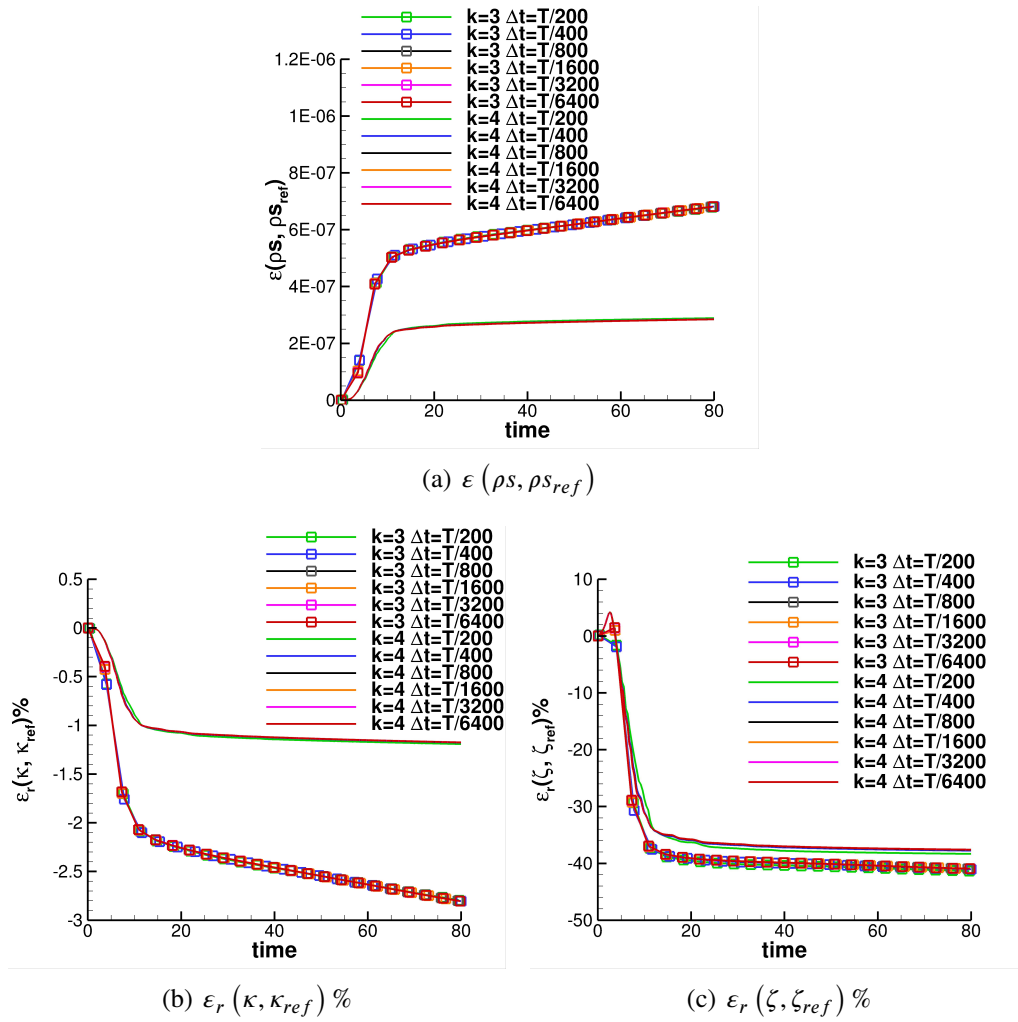


Figure 5: Double shear layers problem – Time refinement study. Simulations performed on the Cartesian grid using the $\mathbb{P}^{3,4}$ DG approximations, the ES numerical flux and the GCNG time integration scheme with different Δt values.

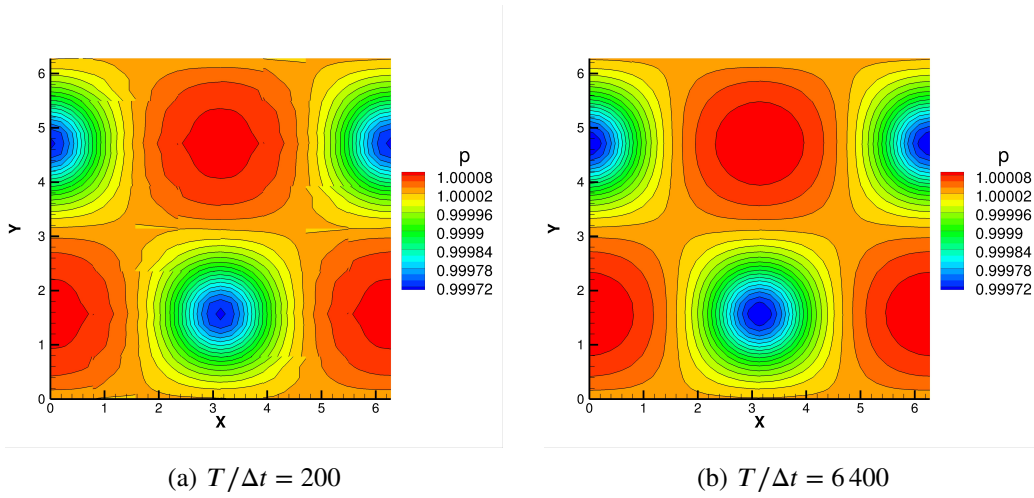
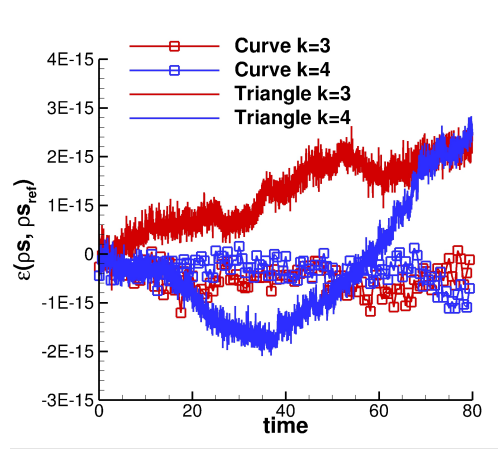
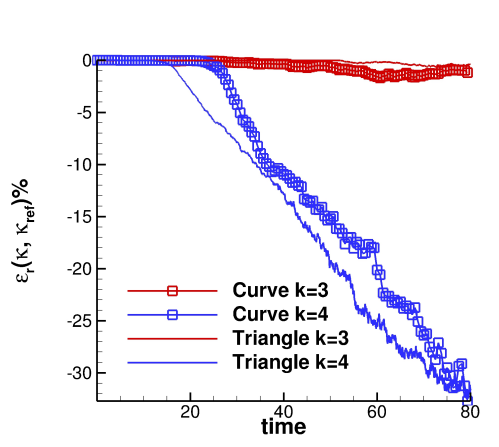


Figure 6: Double shear layers problem – Pressure contours at time $T = 80T_c$ computed on the Cartesian grid using the \mathbb{P}^4 DG approximation, the ES flux and the GCNG time integration scheme with different Δt values.

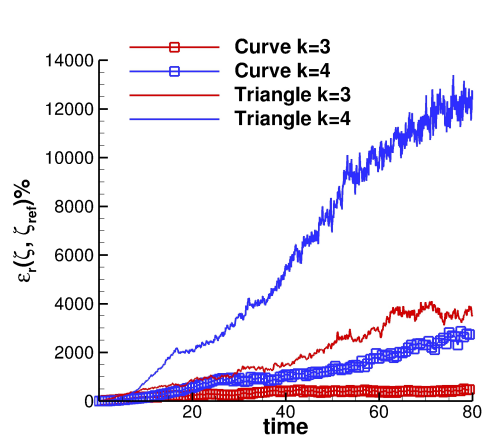
460 To demonstrate the geometrical flexibility of the proposed method, Fig. 7 and
 461 Fig. 8 show the results for the EC and the ES fluxes, respectively, using meshes
 462 made of triangular elements and quadrilateral elements with curved edges. The
 463 grids used, superimposed to the pressure contours, are shown in Fig. 9. The sim-
 464 ulation that uses triangular elements is performed with $\text{CFL} \approx 20$, while, for the
 465 grid with curved edges, this value is ≈ 17 . The numerical experiments essentially
 466 confirm the findings obtained for the Cartesian mesh case. It can be stated that
 467 the method preserves its conservation properties also on unstructured meshes and
 468 without the need of any special treatment.



(a) $\varepsilon(\rho_s, \rho_{s_{ref}})$



(b) $\varepsilon_r(\kappa, \kappa_{ref}) \%$



(c) $\varepsilon_r(\zeta, \zeta_{ref}) \%$

Figure 7: Double shear layers problem – Simulations performed on the meshes made of triangular elements (Triangle) and quadrilateral elements with curved edges (Curve), using the $\mathbb{P}^{3,4}$ DG approximations, the EC numerical flux and the GCNG time integration scheme with $T/\Delta t = 3200$.

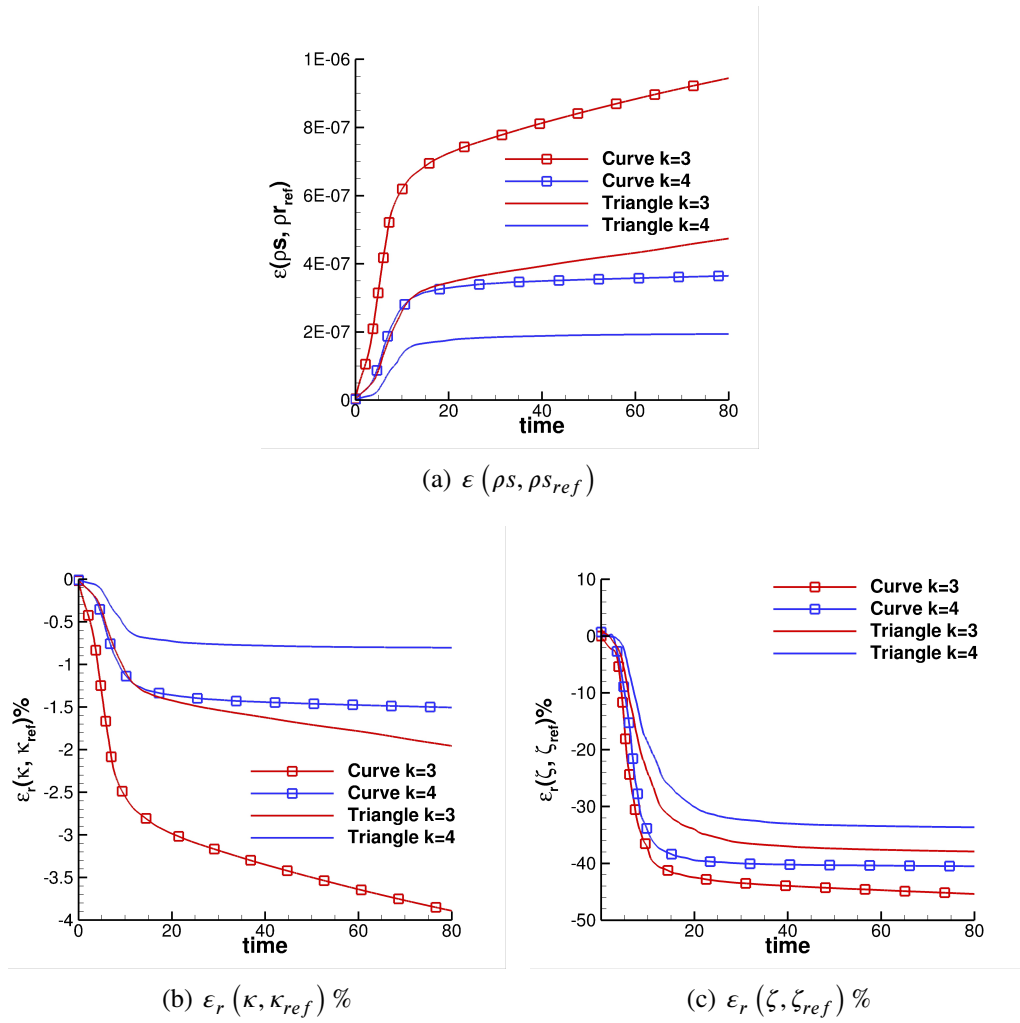


Figure 8: Double shear layers problem – Simulations performed on the meshes made of triangular elements (Triangle) and quadrilateral elements with curved edges (Curve), using the $\mathbb{P}^{3,4}$ DG approximations, the ES numerical flux and the GCNG time integration scheme with $T/\Delta t = 3200$.

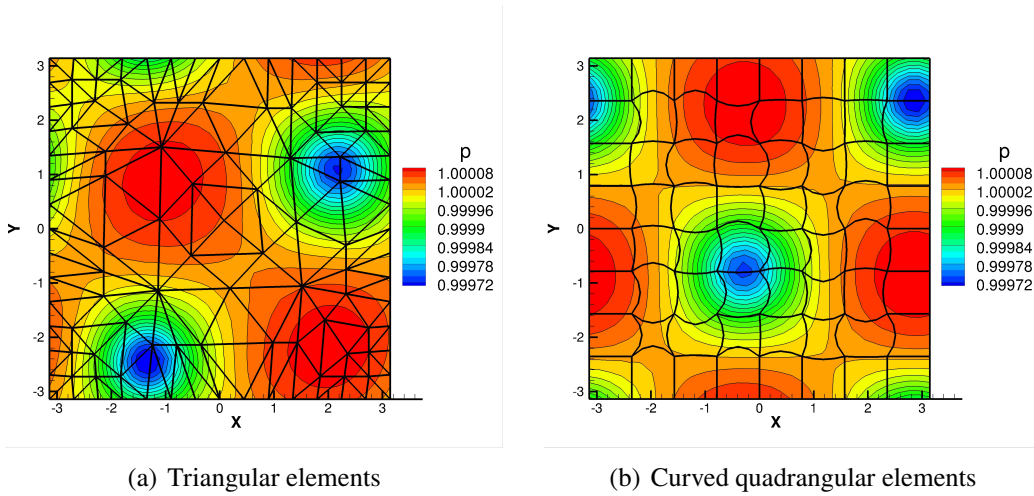


Figure 9: Double shear layers problem – Pressure contours at time $T = 80T_c$. Simulations performed on the meshes made of triangular elements and quadrilateral elements with curved edges using the \mathbb{P}^4 DG approximation, the ES flux and the GCNG time integration scheme with $T/\Delta t = 3200$.

469 *4.3. The Kelvin-Helmholtz instability problem*

470 This section deals with the two-dimensional Kelvin-Helmholtz instability (KHI)
 471 problem parametrized in [32] as a function of the Atwood number $A = (\rho_2 -$
 472 $\rho_1)/(\rho_2 + \rho_1)$. As in the work of Chan et al. [32] an entropy stable DGSEM method
 473 (seventh degree polynomial approximation) was observed to begin to crash for
 474 $A \approx 0.3$, to demonstrate the robustness of the present method a value slightly
 475 larger was used in the following computations, *i.e.*, $A = 1/3$. For the sake of com-
 476 parison with the reference paper, a similar set-up was considered using the entropy
 477 stable ERS flux together with a 32×32 Cartesian uniform grid and polynomial ap-
 478 proximations up to \mathbb{P}^6 .

479 KHI-type flow problems are known to be very sensitive to initial conditions
 480 as well as to the numerical resolution and possible small perturbations. In fact,
 481 the flow evolution is characterized by the generation of small structures becoming
 482 smaller and smaller when increasing the discretization accuracy.

483 It is worth noting that this test case can be considered as a strongly compressible
 484 version of the double shear layer problem with a non-uniform density initialization
 485 and a much higher velocity magnitude (maximum Mach number equal to 0.6 for
 486 $t = 0$). Although the initial condition can be recast in a form similar to Eq. (39),

487 the domain size, $-L \leq x_i \leq L$ with $L = 1$ and the same definitions reported
 488 in [32] are here used

$$\begin{aligned}
 u_1 &= U \left(f(x_2) - \frac{1}{2} \right), \\
 u_2 &= \frac{U}{10} \sin(2\pi x_1), \\
 p &= 1, \\
 \rho &= \rho_1 + f(x_2) (\rho_2 - \rho_1),
 \end{aligned} \tag{40}$$

489 where $f(x_2) = 1/2 [\tanh(15x_2 + 7.5) - \tanh(15x_2 - 7.5)]$, $U = \sqrt{p/\rho_1}$ and $\rho_1 =$
 490 1.

491 Computations have been integrated in time up to $T = 14L/U$, a value larger
 492 than the final time used in [32]. As the dynamics of the problem is quite fast, the
 493 mesh is uniform and the Mach number is high, the computational efficiency of im-
 494 plicit methods was expected not to be very high. Nevertheless, for the $k = 6$ case,
 495 the use of GCNG allows to march in time with a CFL number 7.5 times larger than
 496 the stability limit, *i.e.* 0.2, of the explicit RK35 scheme, see [33], here considered
 497 as a reference solution. Figure 10(a) reports the $\varepsilon(\rho s, \rho s_{ref})$ value as a function
 498 of time. For each time integration scheme solutions are shown up to the largest
 499 admissible CFL_{max} value. For the present numerical set-up and among all the con-
 500 sidered time integrators, *i.e.*, FE, ROS22, ROS33, CNS, GCNG, the ROS33 is
 501 the most stable one with a $CFL_{max} = 2$. For this value, the same scheme also
 502 shows the largest production of entropy on the whole time interval. Concerning
 503 the GCNG, the method outperforms both the SCN ($CFL_{max} = 1$) and the ROS22
 504 ($CFL_{max} = 1.25$) schemes and results, with $CFL_{max} = 1.5$, in a $\varepsilon(\rho s, \rho s_{ref})$ profile
 505 very close to the reference value, the RK35 with $CFL_{max} = 0.2$, or to the result ob-
 506 tained with a smaller time step size ($CFL = 0.5$). Moreover, the SCN and ROS22
 507 schemes proved to be entropy unstable, see the detail in Fig. 10(b). Note that, even
 508 if the ROS33 scheme seems here stable, we are not able to guarantee its entropy
 509 stability. For example, even the ROS58 scheme proves to be entropy unstable, for
 510 large time steps, in Figure 17 of [10]. According to the theory, the stability limit
 511 of the Forward Euler is very low and the method exhibits a nonphysical large drop
 512 of entropy for $t > 8$, see Fig. 10(a). These results highlight how an entropy sta-
 513 ble spatial discretization alone may not guarantee an overall fully discrete entropy
 514 stable method. In fact, entropy production in space can be overwhelmed by the
 515 entropy destruction in time.

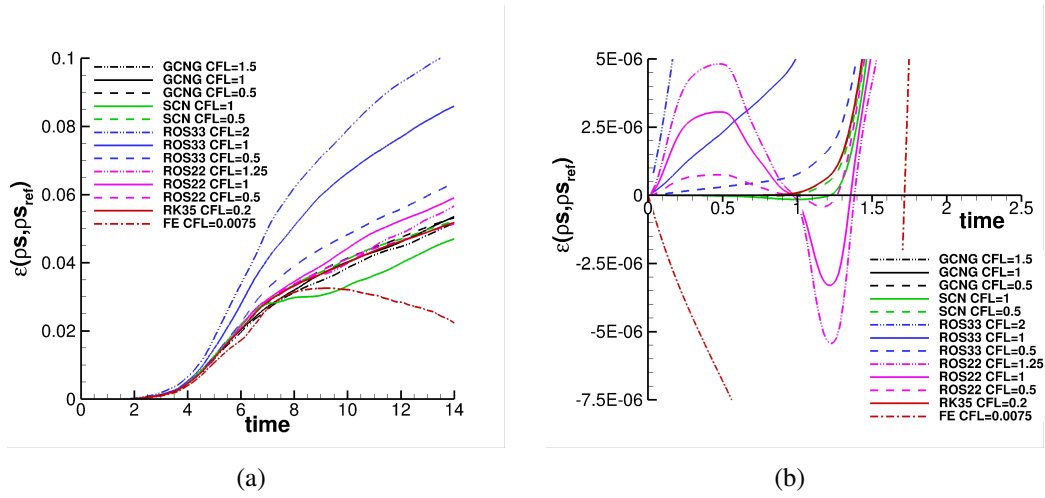


Figure 10: Kelvin-Helmholtz instability problem – Comparison of the $\varepsilon(\rho_s, \rho_{s_{ref}})$ evolution obtained with different time integrators and different CFL values. Simulations performed using the \mathbb{P}^6 DG approximation and the ERS numerical flux.

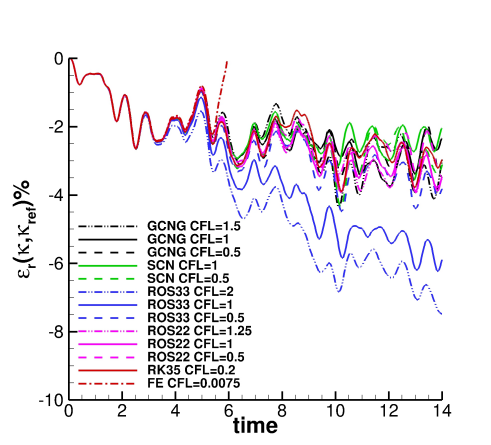


Figure 11: Kelvin-Helmholtz instability problem – Comparison of the $\varepsilon_r(\kappa, \kappa_{ref})\%$ evolution obtained with different time integrators and different CFL values. Simulations performed using the \mathbb{P}^6 DG approximation and the ERS numerical flux.

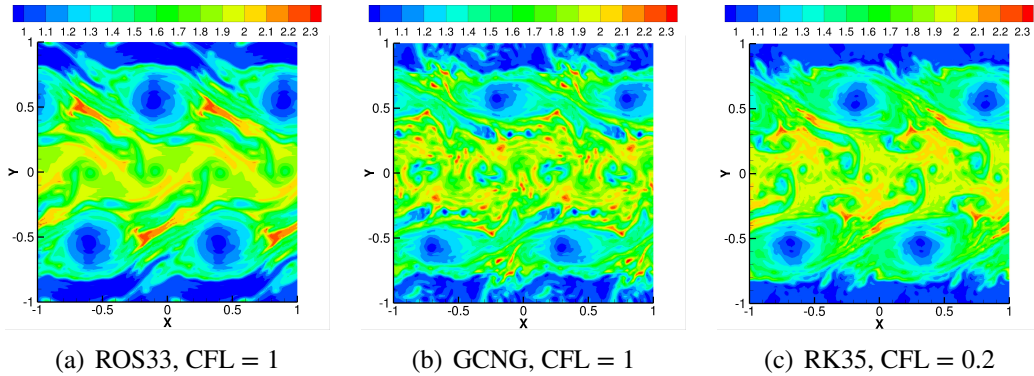


Figure 12: Kelvin-Helmholtz instability problem – Density contours at the final time $T = 14L/U$. Simulations performed using the \mathbb{P}^6 DG approximation, the ERS numerical flux and different time integration schemes.

516 As our objective is to develop a numerical method well suited for the under-
 517 resolved simulation of multiscale phenomena, *e.g.*, in a LES context, it is of partic-
 518 ular interest to investigate the kinetic energy conservation properties of the scheme [19].
 519 As expected, the evolution in time of kinetic energy follows a trend similar to en-
 520 tropy, see Fig. 11, where the $\varepsilon(\kappa, \kappa_{ref})\%$ profile for the GCNG is closer to the
 521 reference curves than the ROS33, which significantly dissipates energy, especially
 522 for large CFL values. As regards the FE, the nonphysical raise of kinetic energy,
 523 shown in Fig. 11, dramatically spoils the solution accuracy, and corresponds to a
 524 drop in entropy, as observed in Fig. 10.

525 Notice that, although the theoretical order of accuracy of ROS33 is larger than
 526 GCNG, *i.e.*, 3 vs. 2, the density contours shown in Figs. 12(a) and 12(b) reveal that
 527 the GCNG delivers a solution containing smaller scales than the ROS33. Obvi-
 528 ously, this behavior does not mean that the GCNG solution is in absolute more ac-
 529 curate, see as a reference the solution obtained with the RK35 scheme in Fig. 12(c).
 530 However, it highlights the enhanced conservation proprieties of the GCNG, with
 531 respects to other schemes, even when using an entropy stable spatial discretization.

532 Finally, Fig. 13 proves that when using the GCNG (CFL= 1) the entropy and
 533 kinetic energy time history of lower polynomial degree discretizations is close to
 534 the $k = 6$ case, although entropy starts to be produced earlier. This behavior is due
 535 to the discontinuities of the solution at the mesh faces, which become larger when
 536 the numerical accuracy is lowered, as they are the only source of entropy when the
 537 ERS flux is coupled with GCNG.

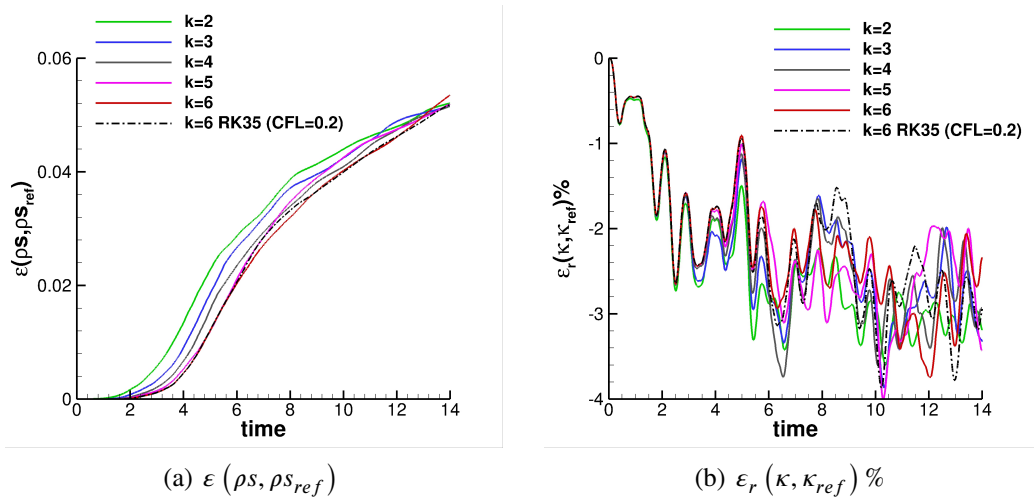


Figure 13: Kelvin-Helmholtz instability problem – Time evolution of $\varepsilon(\rho s, \rho s_{ref})$ and $\varepsilon_r(\kappa, \kappa_{ref})\%$. Simulations performed using the $\mathbb{P}^{2 \rightarrow 6}$ DG approximations, the ERS numerical flux and, if not otherwise indicated, the GCNG time integration scheme.

538 4.4. The shedding flow past a triangular wedge

539 In this section, a simple test case where an inviscid unsteady flow interacts with
 540 boundary conditions is presented. The scope of this flow problem is to testify that
 541 no particular numerical treatment is needed at the boundary when entropy vari-
 542 ables are used. Inspired by [34, 35], the inviscid flow around a triangular wedge
 543 is considered for the free-stream condition $M_\infty = 0.2$. The triangular body im-
 544 mediately generates vortices at sharp corners, even under an inviscid condition,
 545 resulting in a vortex shedding behind the wedge.

546 A natural approach to impose boundary conditions in a DG framework is their
 547 weak enforcement, [5], where properly defined states are used, directly or together
 548 with the internal states, to compute the numerical fluxes at the boundary faces.
 549 These boundary states must be defined according to the condition type and be
 550 consistent with the physical flux. In this flow problem inlet/outlet characteristic-
 551 based conditions are imposed at left/right boundary, symmetry conditions on the
 552 top and bottom boundaries, and the wedge surface is treated as a slip wall.

553 The computational domain consists of an equilateral triangle with side $L = 1$,
 554 placed on the centerline of a rectangular box of size $26L \times 10L$ at a distance $6L$
 555 from the inlet (left) boundary. The simulations were performed using the ERS
 556 flux with the \mathbb{P}^4 approximation on an unstructured mesh made of 5 407 triangular
 557 elements with linear edges. The solution was advanced in time using the GCNG

558 scheme with a time step size equal to $\Delta t = 10^{-2}T_c$ with $T_c = L/U$, where U
559 is the the free-stream velocity magnitude. During iterations, this time step size
560 corresponds to roughly a CFL value of ≈ 2.3 . Figure 14 shows the density contours
561 for two different time levels, $T = 30T_c$ and $T = 50T_c$. A density variation of
562 roughly the 30% is observed for this compressible flow problem. For the $T = 30T_c$
563 snapshot the mesh has been also superimposed on half of the domain for the sake
564 of completeness. Once generated, the eddies are convected downstream, slightly
565 diffused by the quite coarse mesh, and finally interact with the outlet boundary
566 with only a moderate and expected distortion of the flow structure.

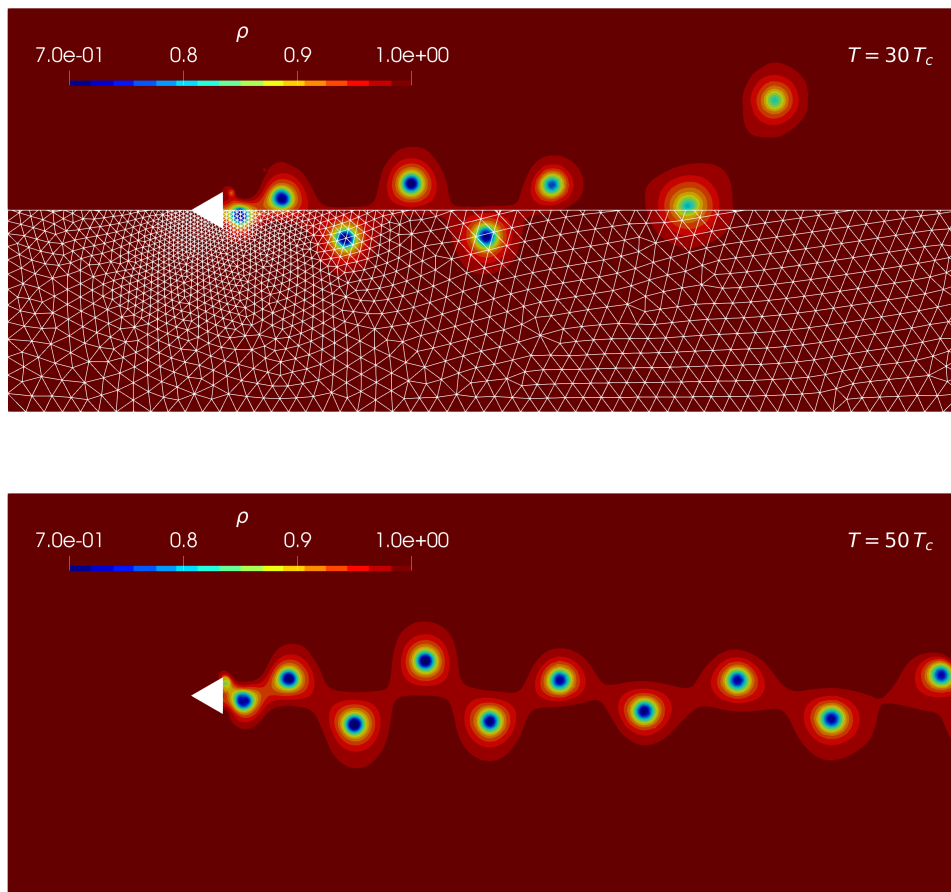


Figure 14: Inviscid flow past a wedge – Density contours, $T = 30T_c$ (top) and $T = 50T_c$ (bottom). Simulation performed on a grid made of 5 407 triangular elements using the \mathbb{P}^4 DG approximation, the ERS numerical flux and the GCNG time integration scheme.

567 4.5. *The receding flow problem*

568 In this section a flow problem where rarefaction is generated by two inviscid
 569 flows receding one from each other is considered. This test case has been exten-
 570 sively studied by Liou [36, 37] and used by Gouasmi et al. in their presentation of
 571 an entropy conserving time integration scheme [17]. The initial condition is given
 572 by two constant states separated by a discontinuity

$$(p, \rho, u) = \begin{cases} (2, 1, -0.4) & \text{if } -0.5 \leq x \leq 0, \\ (2, 1, 0.4) & \text{if } 0 < x \leq 0.5, \end{cases} \quad (41)$$

573 note that these values correspond to the ones used in [17]. This test case exhibits
574 a non-physical temperature rise (overheating) with a spurious entropy generation
575 at the origin that cannot be fixed by simply refining the spatial discretization. Liou
576 proposed to cure this problem by replacing the energy conservation equation with
577 a transport equation for the specific entropy [37]. Unfortunately, this approach
578 does not guarantee for the total energy conservation. Gouasmi et al. demonstrated
579 that this spurious entropy rise is also observed in a fully (both in space and in time)
580 entropy conserving numerical scheme [17].

581 The solutions, here computed up to $T = 0.18$, have been integrated in time with
582 different values for the time-step size $\Delta t = \{10^{-3}, 5 \cdot 10^{-4}, 10^{-4}\}$ and comparing
583 the results of the GCNG with the second-order Rosenbrock-type scheme of Iannelli
584 and Baker (ROS22) [38, 24]. Taking advantage of the symmetry condition set at
585 $x = 0$ the computational domain $x = [0, 0.5]$ is discretized with 50 elements and
586 Dirichlet conditions applied at the right boundary. The temperature profile, with
587 a detail of the symmetry region, is shown for the fully entropy conserving scheme
588 (GCNG and KEEC) and different values of the time step size, $\Delta t = \{10^{-3}, 5 \cdot$
589 $10^{-4}, 10^{-4}\}$, in Fig. 15. It is worth mentioning that in the authors' experience the
590 EC and KEEC flux functions deliver very similar results on several flow cases [10].

591 As expected, due to the essentially non-dissipative nature of the scheme, a
592 solution affected by non-physical oscillations is predicted regardless of the time
593 step size, cf. [10].

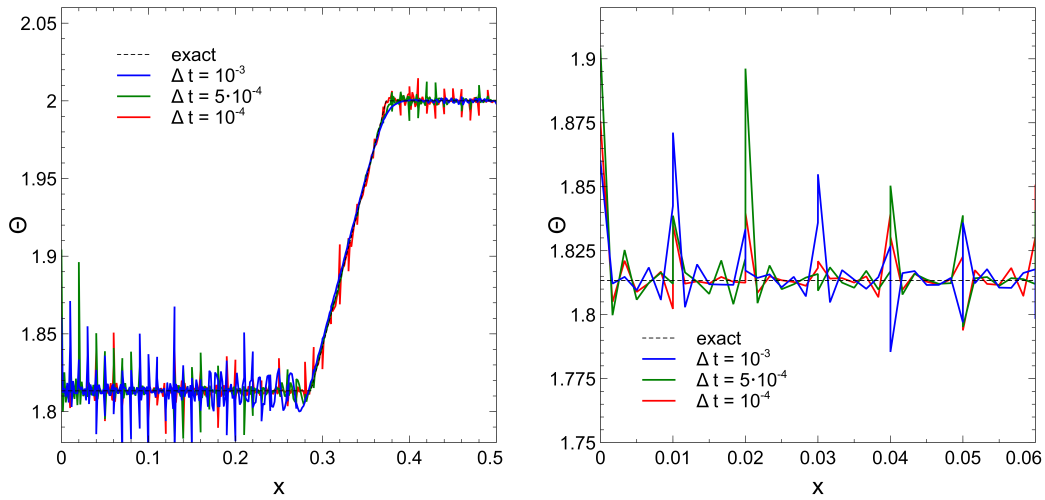


Figure 15: Receding flow problem – Temperature profiles with detail of the symmetry region (right) at $T = 0.18$. Simulations performed on the grid composed by 50 elements using the \mathbb{P}^6 DG approximation, the KEEC numerical flux and the GCNG time integration scheme with different values of the time step size ($\Delta t = \{10^{-3}, 5 \cdot 10^{-4}, 10^{-4}\}$).

594 Figure 16(a) shows a detail of the oscillating entropy profile for the $\Delta t = 10^{-4}$
 595 value and the \mathbb{P}^6 approximation. Fluctuations strongly reduce when an entropy stable
 596 spatial discretization (ERS) and/or the non-entropy-conserving linearly-implicit
 597 ROS22 scheme are used.

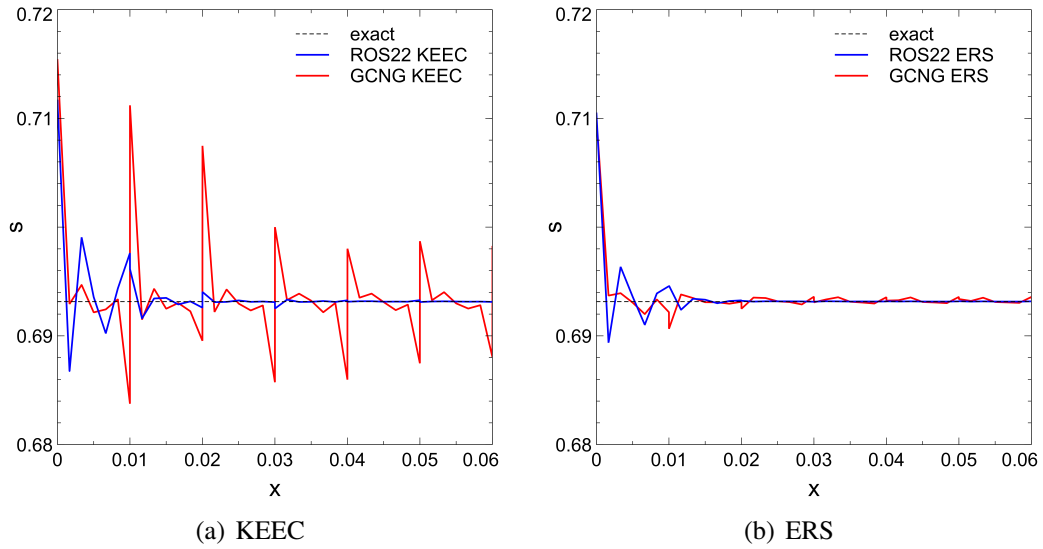


Figure 16: Receding flow problem – Detail of the specific entropy profiles for the receding flow problem at $T = 0.18$. Simulations performed on the grid composed by 50 elements using the \mathbb{P}^6 DG approximation, the KEEC and ERS numerical fluxes and the GCNG and ROS22 time integration schemes with $\Delta t = 10^{-4}$).

598 Temperature profiles are shown in Fig. 17 for the \mathbb{P}^4 approximation and the dif-
 599 ferent values of the time step size when using the ERS flux function together with
 600 the GCNG or the ROS22 time integrators. Oscillations are mainly concentrated
 601 at the symmetry plane, at the foot of the expansion and reduce when reducing the
 602 time step size.

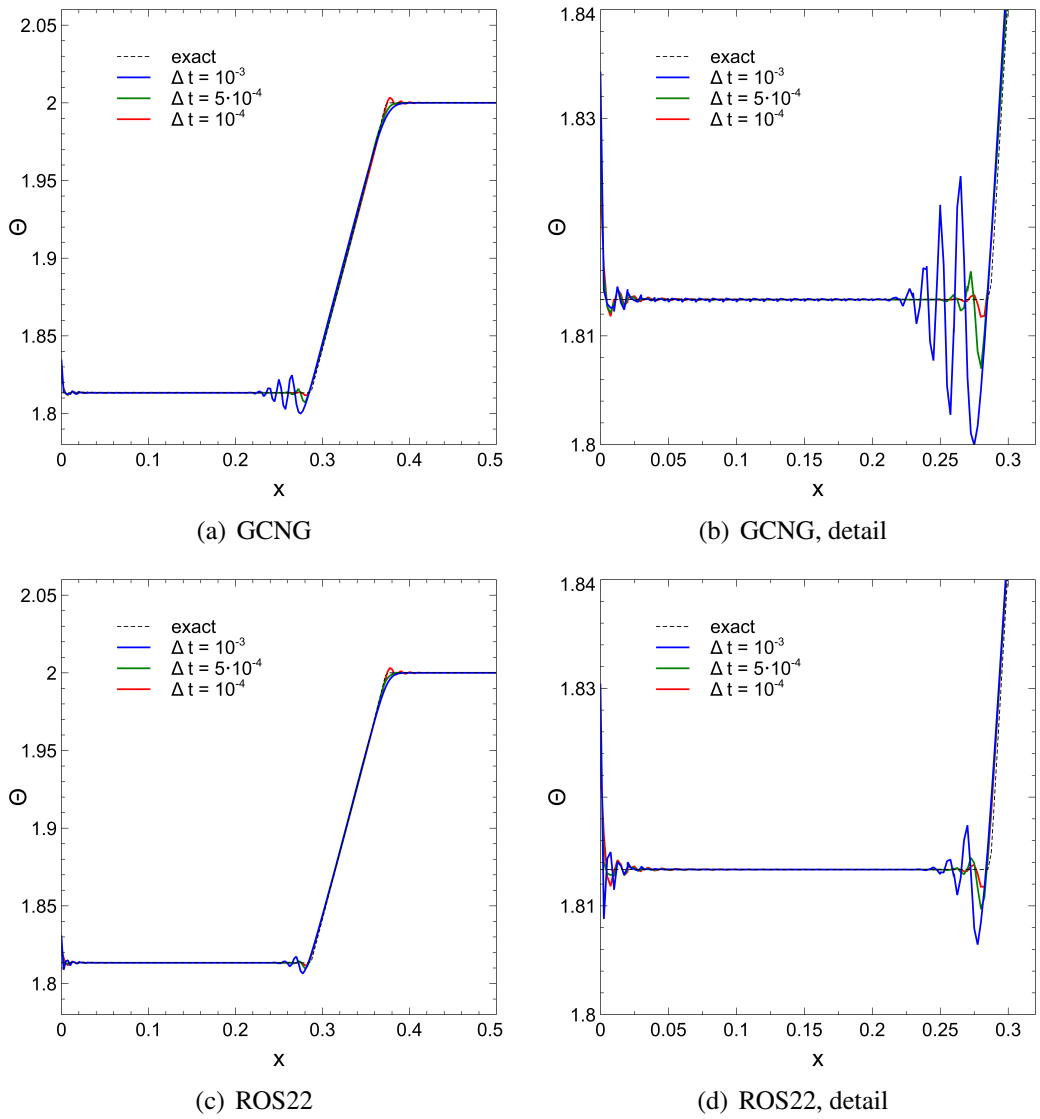


Figure 17: Receding flow problem – Temperature profiles at $T = 0.18$. Simulations performed on the grid composed by 50 elements using the \mathbb{P}^4 DG approximation, the ERS numerical flux and the GCNG and ROS22 time integration schemes with different values of the time step size ($\Delta t = \{10^{-3}, 5 \cdot 10^{-4}, 10^{-4}\}$).

603 Focusing on the use of the GCNG scheme and the ERS flux, when increasing
 604 the accuracy of the spatial discretization from \mathbb{P}^4 to \mathbb{P}^6 , fluctuations reduces as
 605 shown Figure 18. Although pressure is well resolved (Fig. 18(b)), overheating
 606 develops with a slightly under-estimated density value (Fig. 18(c)) and a spurious

607 entropy generation (Fig. 18(d)) at symmetry. This corresponds to the behaviour
 608 observed by Gouasmi et al. in [17].

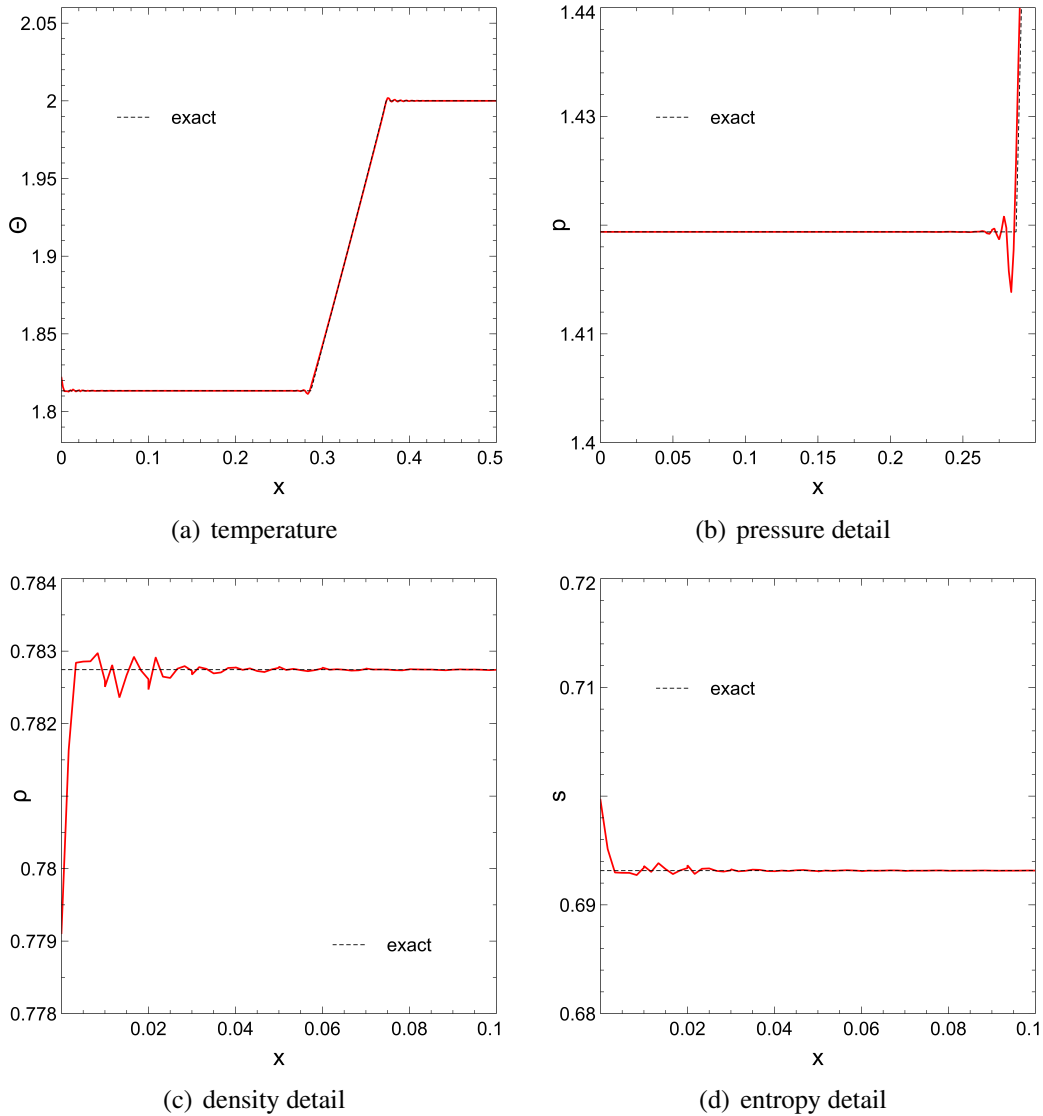


Figure 18: Receding flow problem – Temperature profile for the receding flow problem at $T = 0.18$ with detail of the symmetry region for pressure, density and entropy. Simulations performed on the grid composed by 50 elements using the \mathbb{P}^6 DG approximation, the ERS numerical flux and the GCNG time integration scheme with $\Delta t = 10^{-4}$.

609 *4.6. The Sod shock tube problem*

610 The Sod Shock tube is a Riemann problem for the Euler equations with an
611 initial condition defined as

$$(p, \rho, u) = \begin{cases} (1, 1, 0) & \text{if } -0.5 \leq x \leq 0, \\ (0.1, 0.125, 0) & \text{if } 0 < x \leq 0.5. \end{cases} \quad (42)$$

612 The solution, here computed up to $T = 0.2/\sqrt{\gamma}$, is made of a left-moving rarefac-
613 tion wave, a right-moving contact discontinuity and a right-moving shock wave.
614 The computational domain is spatially discretized with 100 elements and symme-
615 try conditions are applied at boundaries. Computations have been performed with
616 the ERS flux, using the \mathbb{P}^4 approximation and integrating the solution in time with
617 2 000 time steps and the GCNG or the ROS22 [38, 24] schemes.

618 In high-order spatial discretizations flow discontinuities give rise to spurious
619 oscillations that cause stability issues and a loss of accuracy. To cure this prob-
620 lem several strategies to stabilize the solution have been proposed in the literature,
621 *e.g.*, [39, 40, 41, 42]. As in this work the focus is on time integration, to avoid any
622 possible interaction of a discontinuity control algorithm with the solution evolu-
623 tion, we opted not to use any shock-capturing approach during computations. This
624 choice leads to spurious oscillations at discontinuities that also propagate to re-
625 gions where the solution is almost constant, as shown by the density, temperature
626 and velocity profiles in Fig. 19.

627 The results from the ROS22 and the GCNG schemes (same order of accuracy)
628 show an overall similar behaviour and demonstrate that the present method can be
629 considered robust even in presence of flow discontinuities and when an entropy
630 conserving time integration scheme is employed.

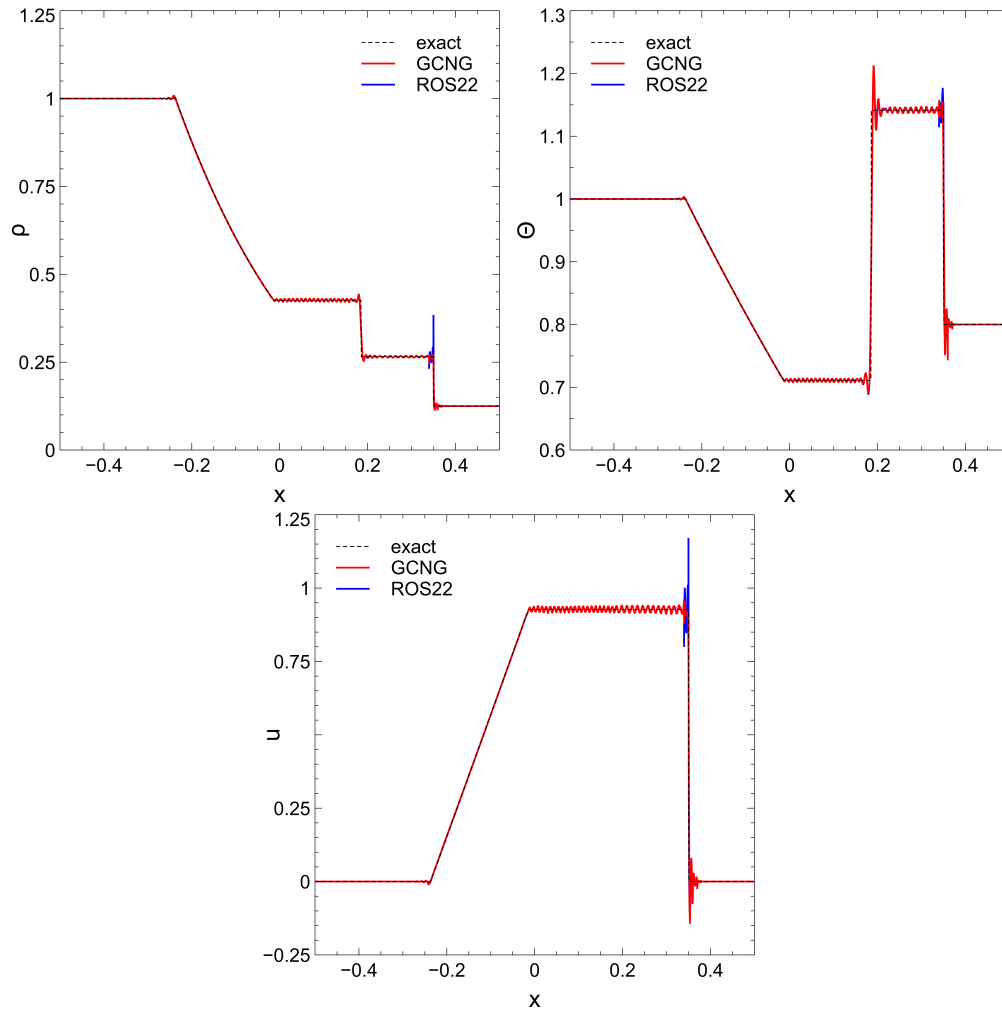


Figure 19: Sod shock tube – Density, temperature and velocity profiles at $T = 0.2/\sqrt{\gamma}$. Simulations performed on the grid composed by 100 elements using the \mathbb{P}^4 DG approximation, the ERS numerical flux and the GCNG and ROS22 time integration schemes.

631 *4.7. The inviscid Taylor-Green vortex*

632 The three-dimensional weakly compressible inviscid Taylor-Green vortex [43]
 633 is here considered as a representative problem to evaluate the performance of the
 634 GCNG scheme for the scale-resolving simulation of turbulent flows. The initial
 635 dimensionless condition is given by

$$\begin{aligned}
u_1 &= U \sin\left(\frac{x_1}{L}\right) \cos\left(\frac{x_2}{L}\right) \cos\left(\frac{x_3}{L}\right), \\
u_2 &= -U \cos\left(\frac{x_1}{L}\right) \sin\left(\frac{x_2}{L}\right) \cos\left(\frac{x_3}{L}\right), \\
u_3 &= 0, \\
p &= 1 + \frac{U^2}{16} \left[\cos\left(\frac{2x_1}{L}\right) + \cos\left(\frac{2x_2}{L}\right) \right] \left[\cos\left(\frac{2x_3}{L}\right) + 2 \right], \\
\rho &= 1,
\end{aligned} \tag{43}$$

636 where $U = M_\infty \sqrt{\gamma}$, $L = 1$ and the “free-stream” Mach number is $M_\infty = 0.1$.
637 The flow problem is solved on the periodic cube $0 \leq x_i \leq 2\pi L$ using two
638 Cartesian grids made of 8^3 (coarse) and 32^3 (fine) elements, respectively. The
639 simulations have been integrated in time up to $T = 20T_c$ with $\text{CFL} \approx 1.4$, where
640 $T_c = L/U$ is the convective time. The inviscid nature of this test case makes
641 it very interesting because an infinite range of scales develop and the numerical
642 solution is under-resolved by definition. Figures 20(a) and 20(b) show the time
643 history of $\varepsilon(\rho_s, \rho_{s_{ref}})$ computed with the fine and the coarse grid, respectively,
644 and several DG approximations. These plots distinctly show that a “true” entropy
645 preserving simulation is possible only if the two entropy conserving schemes, EC
646 in space and GCNG in time, are used together. It is worth noting that the computa-
647 tions performed by coupling the ROS33 scheme with the EC or the ERS numerical
648 fluxes deliver a final value of $\varepsilon(\rho_s, \rho_{s_{ref}})$ of the same order of magnitude (10^{-4}).
649 This result suggests that the evolution of ρ_s is significantly affected by the time in-
650 tegration scheme. However, surprisingly, the ERS results seem almost insensitive
651 to the choice of the time integrator.

652 These findings demonstrate the difficulty in *a priori* identifying the trend of
653 entropy when a not provable entropy conserving scheme is used, here the ROS33.
654 In fact, in the authors’ experience, for a schemes like the ROS33, the entropy pro-
655 duction, and possible destruction, depends on the specific features of the numerical
656 solution.

657 Figures 20(c) and 20(d) report the time history of the relative percentage varia-
658 tion of kinetic energy and confirm that this quantity is much better conserved when
659 the fully entropy conserving scheme uses odd DG approximations ($\mathbb{P}^{3,5}$) rather
660 than even ones ($\mathbb{P}^{4,6}$), cf. Sec. 4.2. Moreover, although the ROS33 is formally one
661 order more accurate than the GCNG, it is observed that κ is better preserved by the
662 last scheme. In fact, as already noted, the conservation of entropy has a positive

663 influence in the preservation of kinetic energy (κ should be perfectly conserved
 664 for $M_\infty \rightarrow 0$).

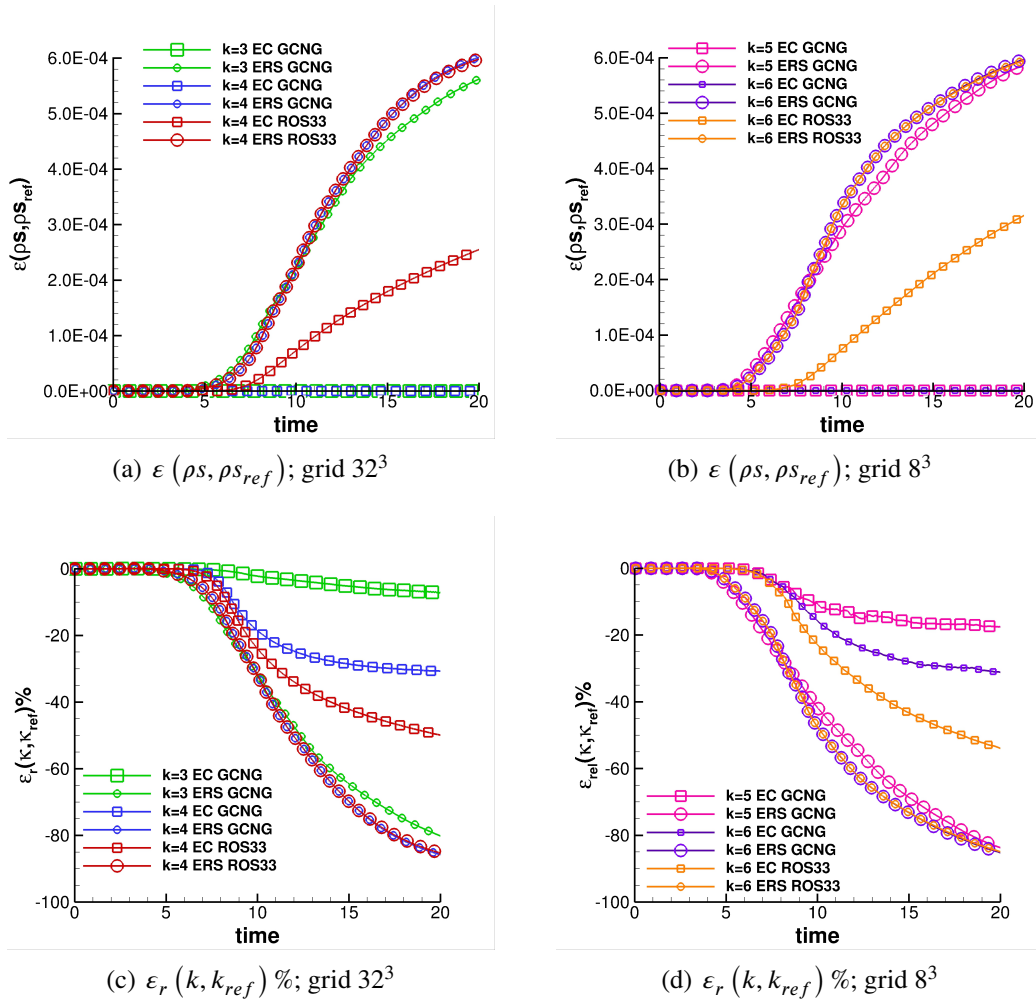


Figure 20: Taylor-Green vortex problem – Time evolution of $\varepsilon(\rho_S, \rho_{S_{ref}})$ and $\varepsilon_r(k, k_{ref}) \%$. Simulations performed on the fine grid using the $\mathbb{P}^{3,4}$ DG approximations (left column) and on the coarse grid using the $\mathbb{P}^{5,6}$ DG approximations (right column), the EC and ERS numerical fluxes and the GCNG and ROS33 time integration schemes.

665 Conclusion

666 In this article a fully discrete entropy conserving/stable numerical method for
 667 the solution of the Euler equations has been presented. The method uses a DG spa-

668 tial discretization and a modified Crank-Nicolson time integration scheme. The en-
669 tropy conserving time integrator, originally proposed in the context of FV schemes,
670 was adapted to a DG discretization in entropy variables theoretically demonstrating
671 the fulfilment of entropy conservation regardless of the time step size. The conser-
672 vation and stability properties have been numerically corroborated by computing
673 several unsteady compressible flow problems, also considering different types of,
674 possibly curved, mesh cells.

675 Future work will be devoted to the solution of the Navier–Stokes equations us-
676 ing the present entropy stable numerical framework with the purpose of addressing
677 scale–resolving simulations of turbulent flows, *e.g.*, DNS, LES.

678 References

- 679 [1] P. G. LeFloch, J. M. Mercier, C. Rohde, Fully discrete, entropy conserva-
680 tive schemes of arbitrary order, *SIAM Journal on Numerical Analysis* 40 (5)
681 (2003) 1968–1992.
- 682 [2] E. Tadmor, Entropy stability theory for difference approximations of nonlin-
683 ear conservation laws and related time-dependent problems, *Acta Numerica*
684 12 (2003) 451–512.
- 685 [3] U. S. Fjordholm, S. Mishra, E. Tadmor, Arbitrarily high-order accurate en-
686 tropy stable essentially nonoscillatory schemes for systems of conservation
687 laws, *SIAM Journal on Numerical Analysis* 50 (2) (2012) 544–573.
- 688 [4] F. Bassi, L. Botti, A. Colombo, D. A. Di Pietro, P. Tesini, On the flexibility of
689 agglomeration based physical space discontinuous Galerkin discretizations,
690 *Journal of Computational Physics* 231 (1) (2012) 45–65.
- 691 [5] F. Bassi, L. Botti, A. Colombo, A. Crivellini, A. Ghidoni, F. Massa, On
692 the development of an implicit high-order discontinuous Galerkin method
693 for DNS and implicit LES of turbulent flows, *European Journal of Mechan-*
694 *ics, B/Fluids* 55 (2016) 367–379. doi:10.1016/j.euromechflu.2015.
695 08.010.
- 696 [6] C. de Wiart, K. Hillewaert, L. Bricteux, G. Winckelmans, Implicit LES of
697 free and wall-bounded turbulent flows based on the discontinuous Galerkin/
698 symmetric interior penalty method, *Int. J. Numer. Methods Fluids* 78 (6)
699 (2015) 335–354. doi:10.1002/flid.4021.

- 700 [7] M. de la Llave Plata, V. Couaillier, M.-C. le Pape, On the use of a high-
701 order discontinuous Galerkin method for DNS and LES of wall-bounded
702 turbulence, *Computers and Fluids* 176 (2018) 320–337. doi:10.1016/j.
703 compfluid.2017.05.013.
- 704 [8] G. J. Gassner, A kinetic energy preserving nodal discontinuous Galerkin
705 spectral element method, *International Journal for Numerical Methods in*
706 *Fluids* 76 (1) (2014) 28–50.
- 707 [9] G. J. Gassner, A. R. Winters, D. A. Kopriva, Split form nodal discontinuous
708 Galerkin schemes with summation-by-parts property for the compressible
709 Euler equations, *Journal of Computational Physics* 327 (2016) 39 – 66.
- 710 [10] A. Colombo, A. Crivellini, A. Nigro, On the entropy conserving/stable im-
711 plicit DG discretization of the Euler equations in entropy variables, *Com-
712 puters & Fluids* 232 (2022) 105198. doi:https://doi.org/10.1016/j.
713 compfluid.2021.105198.
- 714 [11] F. Ismail, P. Roe, Affordable, entropy-consistent Euler flux functions II:
715 Entropy production at shocks, *Journal of Computational Physics* 228 (15)
716 (2009) 5410–5436.
- 717 [12] P. Chandrashekar, Kinetic energy preserving and entropy stable finite volume
718 schemes for compressible Euler and Navier-Stokes equations, *Communica-
719 tions in Computational Physics* 14 (5) (2013) 1252–1286.
- 720 [13] H. Ranocha, G. J. Gassner, Preventing pressure oscillations does not fix local
721 linear stability issues of entropy-based split-form high-order schemes (2020).
722 arXiv:2009.13139.
- 723 [14] L. Friedrich, G. Schnücke, A. R. Winters, D. C. D. R. Fernández, G. J.
724 Gassner, M. H. Carpenter, Entropy Stable Space–Time Discontinuous
725 Galerkin Schemes with Summation-by-Parts Property for Hyperbolic Con-
726 servation Laws, *Journal of Scientific Computing* 80 (1) (2019) 175–222.
- 727 [15] C. Lozano, Entropy production by explicit Runge–Kutta schemes, *Journal of*
728 *Scientific Computing* 76 (1) (2018) 521–564.
- 729 [16] C. Lozano, Entropy production by implicit Runge–Kutta schemes, *Journal of*
730 *Scientific Computing* 79 (3) (2019) 1832–1853.

- 731 [17] A. Gouasmi, S. M. Murman, K. Duraisamy, Entropy conservative schemes
732 and the receding flow problem, *Journal of Scientific Computing* 78 (2) (2019)
733 971–994. doi:10.1007/s10915-018-0793-8.
- 734 [18] P. K. Subbareddy, G. V. Candler, A fully discrete, kinetic energy consis-
735 tent finite-volume scheme for compressible flows, *Journal of Computational*
736 *Physics* 228 (5) (2009) 1347–1364. doi:https://doi.org/10.1016/j.
737 jcp.2008.10.026.
- 738 [19] D. Flad, G. Gassner, On the use of kinetic energy preserving DG-schemes
739 for large eddy simulation, *Journal of Computational Physics* 350 (2017) 782–
740 795.
- 741 [20] T. Hughes, L. Franca, M. Mallet, A new finite element formulation for com-
742 putational fluid dynamics: I. Symmetric forms of the compressible Euler and
743 Navier-Stokes equations and the second law of thermodynamics, *Computer*
744 *Methods in Applied Mechanics and Engineering* 54 (2) (1986) 223 – 234.
- 745 [21] T. Chen, C.-W. Shu, Entropy stable high order discontinuous Galerkin meth-
746 ods with suitable quadrature rules for hyperbolic conservation laws, *Journal*
747 *of Computational Physics* 345 (2017) 427 – 461.
- 748 [22] T. Chen, C.-W. Shu, Review of Entropy Stable Discontinuous Galerkin Meth-
749 ods for Systems of Conservation Laws on Unstructured Simplex Meshes,
750 *CSIAM Transactions on Applied Mathematics* 1 (1) (2020) 1–52.
- 751 [23] S. Balay, S. Abhyankar, M. F. Adams, J. Brown, P. Brune, K. Buschelman,
752 L. Dalcin, A. Dener, V. Eijkhout, W. D. Gropp, D. Kaushik, M. G. Knepley,
753 D. A. May, L. C. McInnes, R. T. Mills, T. Munson, K. Rupp, P. Sanan, B. F.
754 Smith, S. Zampini, H. Zhang, H. Zhang, PETSc Web page (2018).
755 URL <http://www.mcs.anl.gov/petsc>
- 756 [24] F. Bassi, L. Botti, A. Colombo, A. Ghidoni, F. Massa, Linearly im-
757 plicit Rosenbrock-type Runge-Kutta schemes applied to the Discontinuous
758 Galerkin solution of compressible and incompressible unsteady flows, *Com-
759 puters and Fluids* 118 (2015) 305–320. doi:10.1016/j.compfluid.2015.
760 06.007.
- 761 [25] G. Noventa, F. Massa, S. Rebay, F. Bassi, A. Ghidoni, Robustness and ef-
762 ficiency of an implicit time-adaptive discontinuous Galerkin solver for un-

- 763 steady flows, *Computers & Fluids* 204 (2020) 104529. doi:[https://doi.](https://doi.org/10.1016/j.compfluid.2020.104529)
764 [org/10.1016/j.compfluid.2020.104529](https://doi.org/10.1016/j.compfluid.2020.104529).
- 765 [26] J. Gottlieb, C. Groth, Assessment of Riemann solvers for unsteady one-
766 dimensional inviscid flows of perfect gases, *Journal of Computational*
767 *Physics* 78 (2) (1988) 437–458.
- 768 [27] H. Yee, N. Sandham, M. Djomehri, Low dissipative high order shock-
769 capturing methods using characteristic-based filters, *Journal of Computa-*
770 *tional Physics* 150 (1999) 199–238.
- 771 [28] C. Hu, C. Shu, Weighted essentially non-oscillatory schemes on triangular
772 meshes, *Journal of Computational Physics* 150 (1999) 97–127.
- 773 [29] L. Wang, D. Mavriplis, Implicit solution of the unsteady euler equations for
774 high-order accurate discontinuous Galerkin discretizations, *Journal of Com-*
775 *putational Physics* 225 (2007) 1994–2015.
- 776 [30] J. B. Bell, P. Colella, H. M. Glaz, A second-order projection method for the
777 incompressible Navier-Stokes equations, *Journal of Computational Physics*
778 85 (2) (1989) 257–283.
- 779 [31] M. Tavelli, M. Dumbser, A staggered space–time discontinuous Galerkin
780 method for the incompressible Navier–Stokes equations on two-dimensional
781 triangular meshes, *Computers & Fluids* 119 (2015) 235–249.
- 782 [32] J. Chan, H. Ranocha, A. M. Rueda-Ramírez, G. Gassner, T. Warburton, On
783 the entropy projection and the robustness of high order entropy stable Dis-
784 continuous Galerkin schemes for under-resolved flows, *Frontiers in Physics*
785 10.
- 786 [33] R. J. Spiteri, S. J. Ruuth, A new class of optimal high-order strong-stability-
787 preserving time discretization methods, *SIAM Journal on Numerical Analy-*
788 *sis* 40 (2) (2002) 469–491.
- 789 [34] L. Wang, D. J. Mavriplis, Adjoint-based h - p adaptive discontinuous Galerkin
790 methods for the 2D compressible Euler equations, *J. Comput. Phys.* 228 (20)
791 (2009) 7643–7661.

- 792 [35] H. Luo, H. Segawa, M. R. Visbal, An implicit discontinuous Galerkin method
793 for the unsteady compressible Navier–Stokes equations, *Computers & Flu-*
794 *ids* 53 (2012) 133–144. doi:[https://doi.org/10.1016/j.compfluid.](https://doi.org/10.1016/j.compfluid.2011.10.009)
795 2011.10.009.
- 796 [36] M.-S. Liou, Why is the overheating problem difficult: The role of entropy,
797 in: 21st AIAA Computational Fluid Dynamics Conference. doi:10.2514/
798 6.2013-2697.
- 799 [37] M.-S. Liou, The root cause of the overheating problem, in: 23rd AIAA Com-
800 putational Fluid Dynamics Conference. doi:10.2514/6.2017-4107.
- 801 [38] G. Iannelli, A. Baker, A stiffly-stable implicit Runge–Kutta algorithm for
802 CFD applications, AIAA Paper 88-0416.
- 803 [39] P.-O. Persson, J. Peraire, Sub-cell shock capturing for discontinuous Galerkin
804 methods, in: 44th AIAA Aerospace Sciences Meeting and Exhibit, 2006, p.
805 112.
- 806 [40] R. Hartmann, Adaptive discontinuous Galerkin methods with shock-
807 capturing for the compressible Navier-Stokes equations, *International Jour-*
808 *nal for Numerical Methods in Fluids* 51 (9-10) (2006) 1131–1156.
- 809 [41] F. Bassi, L. Botti, A. Colombo, A. Crivellini, N. Franchina, A. Ghidoni,
810 S. Rebay, Very high-order accurate discontinuous Galerkin computation
811 of transonic turbulent flows on aeronautical configurations, in: N. Kroll,
812 H. Bieler, H. Deconinck, V. Couaillier, H. van der Ven, K. Sørensen (Eds.),
813 ADIGMA - A European Initiative on the Development of Adaptive Higher-
814 Order Variational Methods for Aerospace Applications, Vol. 113 of Notes on
815 Numerical Fluid Mechanics and Multidisciplinary Design, Springer Berlin
816 Heidelberg, 2010, pp. 25–38.
- 817 [42] J. Zeifang, A. Beck, A data-driven high order sub-cell artificial viscosity for
818 the discontinuous Galerkin spectral element method, *Journal of Computa-*
819 *tional Physics* 441.
- 820 [43] C.-W. Shu, W.-S. Don, D. Gottlieb, O. Schilling, L. Jameson, Numerical
821 Convergence Study of Nearly Incompressible, Inviscid Taylor–Green Vortex
822 Flow, *Journal of Scientific Computing* 24 (2005) 1–27.